

1 **A fully synthetic three-dimensional human cerebrovascular model based on histological**  
2 **characteristics to investigate the hemodynamic fingerprint of the layer BOLD fMRI signal**  
3 **formation**

4 Mario Gilberto Báez-Yáñez<sup>1</sup>, Wouter Schellekens<sup>1,4</sup>, Alex A. Bhogal<sup>1</sup>, Emiel C.A. Roefs<sup>2</sup>, Matthias  
5 J.P. van Osch<sup>2</sup>, Jeroen C.W. Siero<sup>1,3</sup> and Natalia Petridou<sup>1</sup>

6

7 <sup>1</sup>Translational Neuroimaging Group, Center for Image Sciences, University Medical Center  
8 Utrecht, Utrecht, the Netherlands

9 <sup>2</sup>C.J. Gorter MRI Center, Department of Radiology, Leiden University Medical Center, Leiden, the  
10 Netherlands

11 <sup>3</sup>Spinoza Centre for Neuroimaging Amsterdam, Amsterdam, the Netherlands.

12 <sup>4</sup>Donders Centre for Cognitive Neuroimaging, Radboud UMC, Nijmegen, Netherlands

13

14

15 **Correspondence to:**

16 Mario G. Báez-Yáñez, PhD

17 email: [M.G.Baez-Yanez-2@umcutrecht.nl](mailto:M.G.Baez-Yanez-2@umcutrecht.nl) ; [mbaezy88@gmail.com](mailto:mbaezy88@gmail.com)

18 Translational Neuroimaging Group, Center for Image Sciences, University Medical Center Utrecht,  
19 Room Q.02.4.307, Heidelberglaan 100, 3584 CX, Utrecht, Netherlands, tel: +31 (0) 88 75 50919

20

21 **RUNNING HEADLINE**

22 A human 3D VAMOS model to study the hemodynamic BOLD signal

23

24 **TOTAL WORDS: ----**

25

26

## 27 **ABSTRACT**

28 Recent advances in functional magnetic resonance imaging (fMRI) at ultra-high field ( $\geq 7$  tesla),  
29 novel hardware, and data analysis methods have enabled detailed research on neurovascular  
30 function, such as cortical layer-specific activity, in both human and nonhuman species. A widely  
31 used fMRI technique relies on the blood oxygen level-dependent (BOLD) signal. BOLD fMRI offers  
32 insights into brain function by measuring local changes in cerebral blood volume, cerebral blood  
33 flow, and oxygen metabolism induced by increased neuronal activity. Despite its potential,  
34 interpreting BOLD fMRI data is challenging as it is only an indirect measurement of neuronal  
35 activity.

36 Computational modeling can help interpret BOLD data by simulating the BOLD signal formation.  
37 Current developments have focused on realistic 3D vascular models based on rodent data to  
38 understand the spatial and temporal BOLD characteristics. While such rodent-based vascular  
39 models highlight the impact of the angioarchitecture on the BOLD signal amplitude, anatomical  
40 differences between the rodent and human vasculature necessitate the development of human-  
41 specific models. Therefore, a computational framework integrating human cortical vasculature,  
42 hemodynamic changes, and biophysical properties is essential.

43 Here, we present a novel computational approach: a three-dimensional Vascular Model based  
44 on Statistics (3D VAMOS), enabling the investigation of the hemodynamic fingerprint of the BOLD  
45 signal within a model encompassing a fully synthetic human 3D cortical vasculature and  
46 hemodynamics. Our algorithm generates microvascular and macrovascular architectures based  
47 on morphological and topological features from the literature on human cortical vasculature. By  
48 simulating specific oxygen saturation states and biophysical interactions, our framework  
49 characterizes the intravascular and extravascular signal contributions across cortical depth and  
50 voxel-wise levels for gradient-echo and spin-echo readouts. Thereby, the 3D VAMOS  
51 computational framework demonstrates that using human characteristics significantly affects the  
52 BOLD fingerprint, making it an essential step in understanding the fundamental underpinnings of  
53 layer-specific fMRI experiments.

54

55

56

57

58 **KEYWORDS**

59 7T

60 Cerebrovascular reactivity

61 Computational biophysical modeling

62 Human cortical vascular network

63 Laminar BOLD fMRI

64 Layer fMRI

65 Monte-Carlo simulations

66

67

68

69

70

71

72

73

74

75

76

77

78

79

80

81

82 **ABBREVIATIONS**

83 3D: three-dimensional

84 7T: 7 tesla

85 BOLD: blood oxygenation level-dependent

86 CBF: cerebral blood flow

87 CBV: cerebral blood volume

88 CMRO<sub>2</sub>: oxygen metabolism

89 CSF: cerebrospinal fluid

90 fMRI: functional magnetic resonance imaging

91 GE: gradient echo

92 GM: grey matter

93 HcT: hematocrit

94 SE: spin echo

95 TE: echo time

96 VAMOS: vascular model based on statistics

97 WM: white matter

98

99

100

101

102

103

104

105

## 106 1. INTRODUCTION

107 A widely used functional magnetic resonance imaging (fMRI) technique relies on the blood oxygen  
108 level-dependent (BOLD) signal [Ogawa et al.,1993; Bandettini et al., 1994, 1997]. The BOLD  
109 signal is generated through the combined effects of changes in local deoxygenated-oxygenated  
110 blood, cerebral blood volume (CBV), cerebral blood flow (CBF) and oxygen metabolism (CMRO<sub>2</sub>)  
111 induced by neuronal activity [Ogawa et al.,1993; Bandettini et al., 1994, 1997; Belliveau et al.,  
112 1990; Uludağ et al., 2018].

113 Recent advances in ultra-high field MRI ( $\geq 7$  tesla), novel hardware and fMRI data analysis  
114 methods, allow for the investigation of the cortical and neurovascular function at a high level of  
115 detail, e.g. at the layer-specific activity, in both human and nonhuman species [De Martino et al.,  
116 2013; Goense et al., 2006; Choi et al., 2022; Fracasso et al., 2018; Gülban et al., 2024; Huber et  
117 al., 2017; Kashyap et al., 2018; Vizioli et al., 2021; Siero et al., 2011, 2013; Bause et al., 2020;  
118 Pfaffenrot et al., 2021].

119 While BOLD fMRI offers significant potential for enhancing our understanding of brain function at  
120 the spatial scale of cortical layers, it is important to note that the BOLD signal is only an indirect  
121 measure of brain activity. This indirect mapping comprises a mixture of effects stemming from  
122 hemodynamic changes, the vascular architecture within the sampled volume, and the biophysical  
123 interaction between oxygen saturated blood and tissue [Uludağ et al., 2009]. Given that BOLD  
124 fMRI measures neuronal activation through hemodynamics, its ultimate spatial and temporal  
125 resolution and specificity are dictated by the spatial distribution of hemodynamic changes within  
126 the cortical angioarchitecture, and how these changes evolve over time, i.e. the hemodynamic  
127 fingerprint of the BOLD signal [Zhao et al., 2006; Siero et al., 2011].

128 Computational modeling of the BOLD signal formation has a long story. Starting with the  
129 simulation framework from Ogawa et al [Ogawa et al.,1993]. This model was developed to  
130 understand the susceptibility effect induced by deoxygenated blood and the macroscopic scale  
131 blobs of tissue activity, using a single cylinder model with a predefined angular orientation to mimic  
132 cerebral vessels [Ogawa et al.,1993].

133 More robust and complete computational frameworks succeed it using microspheres and more  
134 complex arrangements of randomly placed oriented cylinder (ROC) models within a voxel. These  
135 complex ROC models aimed to disentangle the macro- and micro-vascular influences on the  
136 BOLD signal, including the impact of pulse sequence choice on BOLD response amplitudes and  
137 vessel size specificity [Fujita N., 2001; Weisskoff et al., 1994; Boxerman et al., 1995; Yablonskiy

138 [et al., 2010](#); [Bieri et al., 2007](#); [Pflugfelder et al., 2011](#)]. Moreover, computational approaches have  
139 enhanced our understanding of MRI signal characteristics. For example, they have demonstrated  
140 the relationship between biophysical interactions, such as the motion of water molecules diffusing  
141 within tissue and the susceptibility-induced effects from changes in vascular oxygen saturation  
142 levels at a mesoscopic scale [[Kiselev et al., 1999, 2018](#); [Kiselev V., 2001](#); [Chausse et al., 2024](#)].

143 Thereby, computational modeling has emerged as a significant research field aiding the  
144 understanding of BOLD fMRI signal formation, offering a means to test hypotheses in ways that  
145 experimental investigations may not always facilitate. It provides comprehensive insight into the  
146 interplay between the cerebral vasculature, intrinsic biophysical properties of the tissues, and  
147 hemodynamic changes. This is particularly relevant for ultra-high magnetic fields and high spatial  
148 resolution fMRI, e.g. submillimeter imaging resolutions, as the signal formation is more specific to  
149 certain sub-regions within the cortex that differ at the mesoscopic scale, for instance, in vascular  
150 density and architecture [[Olman et al., 2012](#); [El-Bouri et al., 2015](#)].

151 Nevertheless, the impact of the three-dimensional (3D) vascular topology, associated  
152 hemodynamics, and their interaction with neighboring tissue on signal formation at the mesoscopic  
153 scale, and the temporal features of the BOLD signal evolution remain elusive [[Norris et al., 2019](#);  
154 [Norris D., 2012](#); [Polimeni et al., 2018](#); [Petridou et al., 2010](#); [Dumoulin et al., 2018](#); [Dumoulin S.,](#)  
155 [2017](#); [Poplawsky et al., 2019](#); [Roefs et al., 2024](#); [Schellekens et al., 2023](#)].

156 Cortical blood vessels in the human brain are organized into well-defined structures with repetitive  
157 topologies [[Duvernoy et al., 1981](#)]. These structures consist of a tree-like arrangement of  
158 penetrating arteries surrounding a central draining vein that collects deoxygenated blood from the  
159 capillary bed toward the superficial pial veins [[Cassot et al., 2009, 2010](#); [Weber et al., 2008](#);  
160 [Schmid et al., 2019](#); [Reichold et al., 2009](#); [Lauwers et al., 2008](#); [Keller et al., 2011](#); [Hirsch et al.,](#)  
161 [2012](#)]. In contrast to the more simplified nonrealistic vascular networks, such as ROC models,  
162 computational simulations utilizing realistic 3D vascular models extracted from the mouse parietal  
163 cortex via two-photon microscopy have highlighted the significant influence of the vascular  
164 architecture and vessel orientation on the measured BOLD signal amplitude with respect to the  
165 main magnetic field [[Gagnon et al., 2015](#); [Báez-Yáñez et al., 2017, 2023](#)]. These findings have  
166 also been corroborated by experimental data [[Viessmann et al., 2019](#); [Fracasso et al., 2018](#)],  
167 demonstrating a phenomenon that could not be observed using nonrealistic vascular models, i.e.  
168 ROC models.

169 Nonetheless, realistic vascular models based on rodents [[Blinder et al., 2010, 2013](#); [Gould et al.,](#)  
170 [2017](#); [Tsai et al., 2009](#)] might not faithfully represent the human cortical vasculature due to

171 interspecies differences in vascular architecture -particularly the artery/vein ratio that feeds and  
172 drains the blood in specific volumetric regions [Duvernoy et al., 1981; Schmid et al., 2019; Uludağ  
173 et al., 2018; Uludağ K., 2023] and in cortical thickness which is larger in humans than in rodents.  
174 Further, the distinct vascular densities and architectures in different cortical regions could  
175 introduce quantitative discrepancies in the simulated BOLD signals for the human brain, and  
176 potentially leading to data misinterpretation [Han et al., 2022; Lorthois et al., 2011].

177 In order to attain a wider understanding of the spatial and temporal hemodynamic fingerprint of  
178 the BOLD signal acquired from human brain scans, it is essential to develop a computational  
179 framework: (I) based upon the architectural layout of the human cortical vasculature, (II) that  
180 includes hemodynamic changes within this simulated vascular network, and (III) that takes the  
181 intrinsic biophysical and magnetic tissue characteristics together with MRI pulse sequence  
182 parameters into account [Gagnon et al., 2015; Markuerkiaga et al., 2021; Havlicek et al., 2017;  
183 Báez-Yáñez et al., 2023; Puckett et al., 2016; Van Horen et al., 2023].

184 In this work, we have developed a computational framework to investigate the laminar  
185 hemodynamic BOLD signal formation based upon a fully synthetic human 3D cortical vascular  
186 model. The so-called 3D VAScular MOdel based on Statistics (VAMOS) algorithm generates both  
187 microvascular and macrovascular angioarchitectures defined by histological, morphological and  
188 topological features obtained from the human cortical vasculature [Duvernoy et al., 1981; Cassot  
189 et al., 2009, 2010; Weber et al., 2008; Schmid et al., 2019]. The microvasculature is generated  
190 through an improved Voronoi tessellation algorithm [Park H., 2021; Báez-Yáñez et al., 2023] and  
191 kernel functions, while the macrovasculature is generated by kernel functions. Both vessel  
192 compartments depend on statistical properties taken from literature values, such as vessel radius,  
193 vessel tortuosity, vessel volume fraction across cortical depth, number of penetrating arteries and  
194 draining veins in a determined volume, cortical penetration dependence for large vessels, among  
195 others [Duvernoy et al., 1981; Cassot et al., 2009, 2010; Weber et al., 2008; Schmid et al., 2019].  
196 This enables simulation of specific oxygen saturation states per vascular compartment and  
197 biophysical interactions, such as diffusion effects of water in tissue, in order to characterize the  
198 intravascular and extravascular signal contribution of diverse vascular architectures to the  
199 gradient-echo (GE) BOLD and spin-echo (SE) BOLD signals, either at the voxel level acquired at  
200 high spatial resolutions or across cortical depth, i.e. layer fMRI. The 3D VAMOS computational  
201 approach can also help to understand the impact of pulse sequence parameters on BOLD signal  
202 changes observed with submillimeter MRI acquisitions.

203

## 204 **2. MATERIAL AND METHODS**

### 205 **2.1 Generation of a fully synthetic human 3D VAScular MOdel based on Statistics – 3D** 206 **VAMOS model**

207 A fully synthetic vascular model is generated using an in-house developed algorithm, and the  
208 statistical properties of the human cortical vasculature are taken from literature that estimated  
209 these by means of histology [Duvernoy et al., 1981; Cassot et al., 2009, 2010; Weber et al., 2008;  
210 Schmid et al., 2019]. First, the microvasculature (consisting of arterioles, capillaries, and venules)  
211 and the macrovasculature (comprising pial arteries and veins, penetrating arteries, and draining  
212 veins) are generated separately. Subsequently, the resulting 3D VAMOS vascular network is fully  
213 connected - by connecting the macrovascular endpoints in the arterial and venous compartments  
214 to the capillary bed, i.e. the microvascular structure. The generation process for each vascular  
215 compartment is described in the following sections.

216

#### 217 **2.1.1 Generation of the microvascular architecture based on Voronoi tessellation and** 218 **kernel functions**

219 To account for the varying cortical thickness and volume fraction occupied by vessels across the  
220 human cortical grey matter, we considered that different cortical areas exhibit different cortical  
221 thicknesses and volume fractions [Fischl et al., 2000]. For instance, the primary visual cortex  
222 spans approximately 2 mm in thickness [Adams et al., 2014; Horton et al., 2018], while the primary  
223 motor cortex presents a thicker cortical depth of approximately 4 mm [Butman et al., 2007].  
224 Therefore, initial parameters in our algorithm to be defined are a customized three-dimensional  
225 space, specifying the dimensions in x, y, and z in millimeters, and a specific vascular volume  
226 fraction, to generate the representative cortical vasculature according to the cortical region being  
227 simulated. The 3D VAMOS allows for the definition of any desired volumetric vascular dimensions,  
228 ranging from hundreds of micrometers to millimeters - thus providing versatility in creating vascular  
229 models that are not limited to represent human vascular networks but could also model mouse  
230 vascular networks, by defining the vascular properties of the studied species (see **Figure 1**).  
231 Within this volumetric space, we assumed full coverage of the cortical vasculature, extending from  
232 the superficial/pial large vessels to the cortical grey-white matter (GM-WM) boundary.

233 The microvasculature was generated using Voronoi tessellation, resulting in a topological network  
234 that resembles a mesh-like structure [Cassot et al., 2009; Lorthois et al., 2011]. Voronoi



235 tessellations have been theoretically shown to effectively represent the capillary bed supplying  
236 brain tissue [[Safaeian et al., 2011](#); [El-Bouri et al., 2015](#)].

237 The simulated volumetric space was divided into a number,  $S$ , of equidistant slabs in the  $xy$ -plane.  
238 The number  $S$  is calculated based on the vascular volume fraction and vessel features, such as  
239 vessel radius. A Voronoi tessellation was generated by fragmenting each of the slabs into tiles  
240 that encompass a given set of seed points [[Park H., 2021](#)]. The distribution of the seed points can  
241 follow any specific distribution across the slab to simulate different capillary densities across  
242 cortical depth [[Schmid et al., 2019](#)]. For example, a Gaussian distribution can be simulated in the  
243  $xz$ -plane or  $yz$ -plane to create larger capillary densities, i.e. a larger density of Voronoi tiles in a  
244 specific part of the slab. This rational follows on that the vessel distribution across cortical depth  
245 is denser in the middle layers compared to the superficial and granular layers. [[Schmid et al.,](#)  
246 [2019](#)].

247 Each slab, then, was tessellated using the linear inequalities formed by perpendicular bisectors  
248 between any two connected points in the Delaunay triangulation, employing an adapted version  
249 of the polytope-bounded Voronoi diagram algorithm [[Park H., 2021](#)]. Once all the slabs contained  
250 the tessellations, joint vessels in the  $i$ -th slab were connected with the nearest (shortest Euclidean  
251 path) adjacent joint vessel of the  $(i+1)$ -th slab. This results in a fully interconnected network  
252 structure consisting of vertices, i.e. microvessel joints, and lines connecting those vertices, i.e.  
253 microvessels. Moreover, to increase complexity and mimic real capillary networks, the vertices  
254 generated by the tessellation are randomly displaced orthogonally to the slab by a small distance,  
255 typically on the order of tens of micrometers. This displacement helps create a volumetric shape  
256 for the components of each slab.

257 To generate a closer resemblance to actual capillary beds, an important characteristic to include  
258 is the tortuosity of the microvessels [[Gould et al., 2017](#); [Risser et al., 2007](#); [Hartung et al., 2018](#)].  
259 The tortuosity ( $\tau$ ) was defined as the ratio of the vessel length between two joint vessel points, i.e.  
260 vertices within the Voronoi tessellation, and the Euclidean distance between those two joint vessel  
261 points (see **Figure 2**),

$$262 \quad \tau = \frac{\text{vessel length}_{\text{vessel joints}}}{\text{Euclidean distance}_{\text{vessel joints}}} \quad (1)$$

263 In order to generate different vessel morphologies that fulfill the tortuosity characteristic, we  
264 implemented an iterative curve generator algorithm that creates plausible vessel morphologies  
265 based on predefined mathematical functions. Hereafter, we will refer to these as kernel functions.  
266 Examples of different tortuosity of the capillary bed are shown in **Figure 2**.

267 Along with the tortuosity, each line on the Voronoi network was assigned a value resembling the  
268 vessel radius. This value was determined by a predefined Gaussian distribution with a desired  
269 mean and standard deviation. The mean and standard deviation values were selected based on  
270 histological definitions dependent on the cortical region of investigation [Weber et al., 2008; Horton  
271 et al., 2018].

272

### 273 **2.1.2 Generation of the macrovascular architecture based on kernel functions**

274 Based on the predefined customized three-dimensional space where the microvascular network  
275 was generated, the macrovascular architecture was constructed. The first step involves  
276 generating the pial arteries and veins. The 3D VAMOS can generate any desired number of pial  
277 arteries and veins; however, their quantity is subject to the defined number of penetrating arteries  
278 and draining veins set as initial parameters based on literature values [Duvernoy et al., 1981].

279 At the top plane of the volumetric space, i.e. at the maximal z-cross-section, seed points were  
280 randomly placed in the xy-plane, constrained only by the defined closer proximity value (~120  
281 micrometers). Subsequently, each seed point was designated to be part of an artery or a vein.  
282 The distribution of labels to the seed points follows the rationale that veins, by first principles, must  
283 be surrounded by arteries, as described by histological data from the primary visual cortex [Adams  
284 et al., 2015]. This rationale does not apply for the mouse model, given the reversed/opposite  
285 artery-vein ratio observed in mouse brain.

286 Next, labeled pial artery seed points were interconnected using kernel functions with predefined  
287 vessel tortuosity and vessel radius. The same process was applied to the labeled pial veins (see  
288 **Figure 3**).

289 After creating the pial vasculature, the subsequent step generates the main branches of the  
290 penetrating arteries and draining veins. The 3D VAMOS facilitates the definition of the cortical  
291 penetration depth for these vessels based on the observations by Duvernoy et al [Duvernoy et al,  
292 1981]. The main penetrating artery or draining vein can be specified to extend to varying depths,  
293 classified as Laminae 1 (L1) to Laminae 5 (L5). This classification corresponds to five equidistant  
294 laminae throughout the cortical depth (z-axis), with L1 positioned closer to the pial surface and L5  
295 nearer to the cortical grey-white matter boundary (see **Figure 3**). Guided by the cortical  
296 penetration depth label, an endpoint of the main branch for each large vessel is aligned parallel to  
297 those of the seed points at the cortical surface and subsequently connected by another predefined  
298 kernel functions.

299 Furthermore, the number of sub-branches, daughters of the main vessel segment, can be  
300 predetermined as an initial parameter for each main vessel branch. These sub-branches were  
301 randomly positioned along the main vessel branch and generated using another set of predefined  
302 kernel functions. The vessel radius of both the penetrating/draining vessel and their sub-branches  
303 adheres to a branching exponent, i.e. Murray's law ( $R_{\text{parent}}^k = R_{\text{daughter1}}^k + R_{\text{daughter2}}^k$  with k values  
304 reported to be between 2 and 3 in both human and rodents; here we selected  $k = 2$ ). Initially  
305 adopting the radius value assigned to the cortical pial surface seed points before gradually  
306 diminishing in radius size across the cortical depth until reaching the endpoints of the main branch  
307 and sub-branches (see **Figure 3**). Consequently, the 3D VAMOS currently generates for each  
308 parent penetrating/draining vessel (main branch) a specified number of daughter vessels  
309 expanding in a radial pattern (sub-branches), resembling a topological tree-like structure [[Cassot  
310 et al., 2009](#)]. The number of sub-branches, sub-branch vessel length and sub-branch tortuosity  
311 can be set to different values dependent on the cortical region of investigation.

312 One last key feature of the 3D VAMOS is the ability to define whether L5 draining veins are either  
313 connected or not at the level of the cortical grey-white matter boundary. When this parameter is  
314 selected, all labeled L5 draining veins are interconnected by predefined kernel functions (see  
315 **Figure 3**).

316

### 317 **2.1.3 Physical connection between vascular compartments**

318 After generating both vascular compartments, i.e. the macrovessels and the microvessels, all the  
319 endpoints of the macrovascular main branches and sub-branches are connected to the nearest  
320 vessel junction of the microvascular compartment using the shortest Euclidean path between  
321 vessel joints, resulting in a fully interconnected network. This key feature allows for hemodynamic  
322 simulations, assuming only boundary conditions manipulation at the blood inlets/outlets sources,  
323 i.e. pial arteries and veins, respectively, and vasodilation changes of certain vessels or specific  
324 vascular compartments [[Lorthois et al., 2011](#)]. This improvement is significant compared to the  
325 SVM [[Báez-Yáñez et al., 2023](#)], where the macrovascular compartment was only superimposed  
326 on the microvasculature without being connected to it.

327

328

329

## 330 **2.2 Simulation of the BOLD signal using the 3D VAMOS accounting for intravascular and** 331 **extravascular signal contributions**

332 The total simulated BOLD signal was calculated by summing the extravascular signal with the  
333 intravascular contributions from arteries and veins:

$$334 \text{ BOLDsignal} = \text{Extravascular}_{\text{signal}} + \text{Intravascular}_{\text{signal(arteries)}} + \text{Intravascular}_{\text{signal(veins)}} \quad (2)$$

335 Simulations shown here were computed for gradient echo (GE) and spin echo (SE), assuming  
336 infinite readout length, at 7T using an echo time of 27 ms and 50 ms, for GE and SE, respectively,  
337 with the main magnetic field oriented parallel to the normal vector of the cortical pial surface.

338

### 339 **2.2.1 Simulation of the arterial and venous intravascular signal contribution**

340 In this study, we assumed the intravascular contribution ( $R2^{(*)}_{\text{dHb}} = R2^{(*)}_{0,\text{in}} + R2_{\text{SO}_2}$ ) to the  
341 BOLD signal to be non-zero for the arterial and venous compartment. This decision was based on  
342 the observation that, at high magnetic fields, the intravascular contribution of the arterial and  
343 venous compartment tends to be significant at specific oxygen saturation levels [Uludag et al,  
344 2009]. In the microvascular compartment, we assumed zero contribution as an intravascular  
345 component, given that the  $R2^{(*)}_{\text{dHb}}$  of the capillaries has not been well-characterized due to the  
346 high heterogeneity in hematocrit levels across the cortical depth and oxygen saturation levels  
347 across the capillary bed [Gould et al., 2017].

348 Therefore, we implemented the intravascular intrinsic arterial and venous contribution for SE as  
349  $1/R2_{0,\text{in}} = T2_{0,\text{in}} (\approx 53 \text{ ms})$ , and for GE as  $1/R2^*_{0,\text{in}} = T2^*_{0,\text{in}} (\approx 10 \text{ ms})$ . The  $R2_{\text{SO}_2}$  component,  
350 for both pulse sequences, depends on oxygen saturation level using the quadratic relation as  
351 defined by Uludag et al. [Uludag et al, 2009], weighted by the corresponding arterial or venous  
352 blood volume fraction (see **Figure 1**).

$$353 \text{ Intravascular}_{\text{signal(arteries or veins)}}(t) \\ 354 = (\text{CBV}_{\text{arteries or veins}}) \cdot \left( e^{-R2^{(*)}_{\text{dHb}} \cdot t} \right) \quad R2^* \text{ for GE and } R2 \text{ for SE} \quad (3)$$

355 Although the intravascular decay rate for both GE and SE is influenced by hematocrit level, we  
356 assumed a constant value of hematocrit across vascular compartments in our simulations ( $\text{Htc} =$   
357  $45\%$ ). This decision requires one degree of freedom less in the hemodynamic simulations.

358

## 359 2.2.2 Simulation of the extravascular signal contribution

### 360 2.2.2.1 Implementation of oxygen saturation levels for each vascular compartment

361 We simulated different oxygen saturation levels per vascular compartment, which were  
362 maintained constant over time, i.e. steady-state oxygen saturation levels were assumed. The  
363 baseline oxygen saturation (SO<sub>2</sub>) values used in the microvascular compartment were dependent  
364 on the oxygen saturation imposed on the veins as follows [Vovenko E., 1999]:

- 365     ▪ SO<sub>2</sub> in arteries (SO<sub>2art</sub>) = 95%;
- 366     ▪ SO<sub>2</sub> in capillaries = SO<sub>2art</sub> - ((SO<sub>2art</sub> - SO<sub>2vein</sub>) / 2);
- 367     ▪ SO<sub>2</sub> in veins (SO<sub>2vein</sub>) = [from 60% to 80% at an interval increment of 1.6%].

368

### 369 2.2.2.2 Simulation of the extravascular signal contribution

370 The extravascular BOLD signal was computed by modelling the interaction of moving spins within  
371 the local magnetic field distortions induced by the different oxygen saturation levels of both the  
372 macro- and micro-vasculature (section 2.2.2.1). We computed local frequency shifts caused by a  
373 vessel segment as the dipolar response of a finite cylinder, presuming negligible effects on the  
374 cylinder extremities [Báez-Yáñez et al., 2017]. The local frequency shift  $\delta\omega(r)$  in [1/s] for each  
375 vessel segment was computed using:

$$376 \quad \delta\omega(r) = \frac{1}{2} \cdot \frac{\gamma}{2\pi} \cdot B_0 \cdot \Delta\chi \cdot \left(\frac{R^2}{r^2}\right) \cdot \cos(2\theta) \cdot \sin^2\psi \quad (4)$$

377 where  $\gamma$  is the hydrogen gyromagnetic ratio = 267.5E6 [rad/(s·T)],  $B_0$  is the main magnetic field  
378 (7 [T]),  $\Delta\chi = 4\pi \cdot 0.276 \text{ ppm} \cdot \text{HcT} \cdot (1 - \text{SO}_2)$  [-] is the susceptibility difference produced by the SO<sub>2</sub>  
379 in the vessel/cylinder and the hematocrit level HcT (= 0.45 [-]) [Pries et al., 1992],  $R$  is the vessel  
380 radius in [ $\mu\text{m}$ ],  $r$  is the Euclidean distance from the center line of the cylinder to a particular spatial  
381 position in the simulation volume in [ $\mu\text{m}$ ],  $\theta$  is the angle between the cylinder and the spatial  
382 position in [rad], and  $\psi$  is the angle between the orientation of the cylinder and the main magnetic  
383 field in [rad].

384 The dephasing experienced by a bulk of diffusing spins ( $N_{\text{spins}}$ ) was simulated using a Monte  
385 Carlo approach over 20 repetitions, with  $5 \cdot 10^7$  spins in each repetition and assuming an isotropic  
386 diffusion coefficient of  $D = 1.2 \text{ } [\mu\text{m}^2/\text{ms}]$  [Kiselev V., 2001]. It is worth noting that, in order to  
387 increase the statistical averaging/power of the simulated BOLD signals, a different 3D VAMOS  
388 vascular model was generated for each repetition using the same initial vascular parameters.

389 Thus, the morphology of the vascular model varies in each repetition –similar to averaging the  
390 BOLD signal contribution from several voxels.

391 The calculation of the spin dephasing was obtained through,

$$392 \quad \varphi(t) = \int_0^t \delta\omega(x(t)) dt \quad (5)$$

393 where  $\varphi(t)$  is the phase acquired during the simulation time  $t$  and  $\delta\omega(x(t))$  is the local frequency  
394 shift at spin position  $x$  at each time-step  $t$ . The phasing experienced for each spin was stored  
395 across all simulation time-steps (time step = 0.025 ms). For SE sequences, the acquired phase  
396 during the echo time was multiplied by -1 (change in polarity) after  $TE/2$ , simulating the effect of  
397 the 180-degree refocusing radiofrequency pulse. Using equation (6) we can obtain the normalized  
398 extravascular BOLD signal.

$$399 \quad \text{Extravascular}_{\text{signal}}(t) = (1 - \text{CBV}_{\text{arteries+veins}}) \cdot \left[ \left( \frac{1}{N_{\text{spins}}} \sum^{N_{\text{spins}}} e^{-i\varphi(t)} \right) \cdot e^{-R2_0^{(*)} \cdot t} \right] \quad (6)$$

400 Where  $R2_0^{(*)} = 1/T2_0^{(*)}$  is the intrinsic decay rate in cortical tissue, and  $R2'$ , expanded in the term  
401 inside the parenthesis, is the decay rate induced by the interaction of the diffusing spins in a local  
402 inhomogeneous frequency field. We used the intrinsic tissue  $T2_0^*$  ( $\approx 28$  ms) relaxation time for GE  
403 and the intrinsic tissue  $T2_0$  ( $\approx 50$  ms) relaxation time for SE according to the nonlinear relationship  
404 given by Khajehim et. al. [Khajehim et al., 2017] for cortical grey matter at 7T.

405 To confine spins within the simulation space, voxel boundary conditions were set to infinite space.  
406 Spins exiting the “voxel” re-entered the imaging volume on the opposite side, preserving their  
407 magnetization history. However, spins reaching the cortical pial surface and WM/GM boundary  
408 were considered invalid iterations and reiterations were performed. Additionally, spin exchange  
409 between vascular compartments was prohibited, establishing an impermeable vascular network.

410

### 411 **2.3 GE $R2^*$ and GE BOLD signal change, and SE $R2$ and SE BOLD signal change across** 412 **cortical depth**

413 The BOLDsignal and the corresponding GE  $R2^*$  and SE  $R2$  were computed using their respective  
414 echo time as described in section 2.2. Given that the behavior of the MR signal, in general,  
415 presents oscillations due to its multi-exponential nature [Kiselev V., 2001], we simply approximate  
416 the  $R2^{(*)}$  decay rate value fitting a polynomial of degree one, i.e. a linear fit, on the natural logarithm

417 of the BOLDsignal,  $R2^{(*)} = \frac{\ln(\text{BOLDsignal})}{t}$ , for GE and SE, respectively. The BOLD signal change in  
418 [%] was defined as the relative change using the 60% oxygen saturation state as the  
419 reference/baseline condition ( $\text{SO}_{2\text{vein}} = 60\%$ ), i.e.,

$$420 \quad \Delta\text{BOLD} = \left( \frac{\text{BOLDsignal}(\text{SO}_{2\text{vein}}, t)}{\text{BOLDsignal}(\text{SO}_{2\text{vein}=60\%}, t)} - 1 \right) \times 100 \quad (7)$$

421 Each simulated model was divided into fifteen layers to characterize the behavior across cortical  
422 depth. These layers do not represent or resemble any realistic definition of cortical layers obtained  
423 through histological samples.

424

#### 425 **2.4 Using randomly oriented cylinder (ROC) models to simulate cortical layer BOLD signals**

426 In order to demonstrate the advantages of using a realistic 3D vascular model, we generated a  
427 composite vascular model using ROCs, as displayed in **Figure 2**, to simulate the laminar BOLD  
428 contribution. Macrovascular ROC models were simulated using cylinder/vessel radius sizes  
429 ranging from 10  $\mu\text{m}$  to 40  $\mu\text{m}$ , and microvascular ROC models were simulated using  
430 cylinder/vessel radius sizes within the range of 0.5  $\mu\text{m}$  to 6  $\mu\text{m}$ , as shown in **Figure 2**. We imposed  
431 a volume fraction dependent on cortical depth for both macrovascular and microvascular ROC  
432 models. Thus, simulating a cortical thickness of 1 mm isotropic, we divided it into eight equidistant  
433 layers. The volume fraction of each layer depends on the vascular compartment. The  
434 macrovascular ROC model follows a volume fraction of 3% at the cortical surface, decreasing its  
435 value across cortical depth, as depicted in **Figure 2**. The microvascular ROC model intends to  
436 simulate a Gaussian distribution, with a 3% value in the middle layers and decreasing values  
437 toward the cortical surface and the GM/WM boundary, as shown in **Figure 2**. The oxygen  
438 saturation levels used were selected to match the values typically found in veins –  $\text{SO}_2 = 60\%$  to  
439 80% (see Section 2.2.2.1). Moreover, we employed the same biophysical properties of tissue as  
440 described previously.

441

442

443

444

445



### 446 3. RESULTS

447 To demonstrate the capabilities and versatility of the 3D VAMOS computational framework, we  
448 generated three different vascular models – one mouse vascular model (parietal cortex) and two  
449 human vascular models (primary visual cortex and primary motor cortex) (see **Figure 1**).

450 These 3D VAMOS models were confined to a simulation space of an approximately  $1 \times 1 \times 1 \text{ mm}^3$   
451 for the mouse model (**Figure 1.A**);  $2 \times 2 \times 2 \text{ mm}^3$  for the primary visual cortex (**Figure 1.B**), and  $4$   
452  $\times 4 \times 4 \text{ mm}^3$  for the primary motor cortex (**Figure 1.C**). These vascular models represent the  
453 corresponding cortical thickness of each brain region and species.

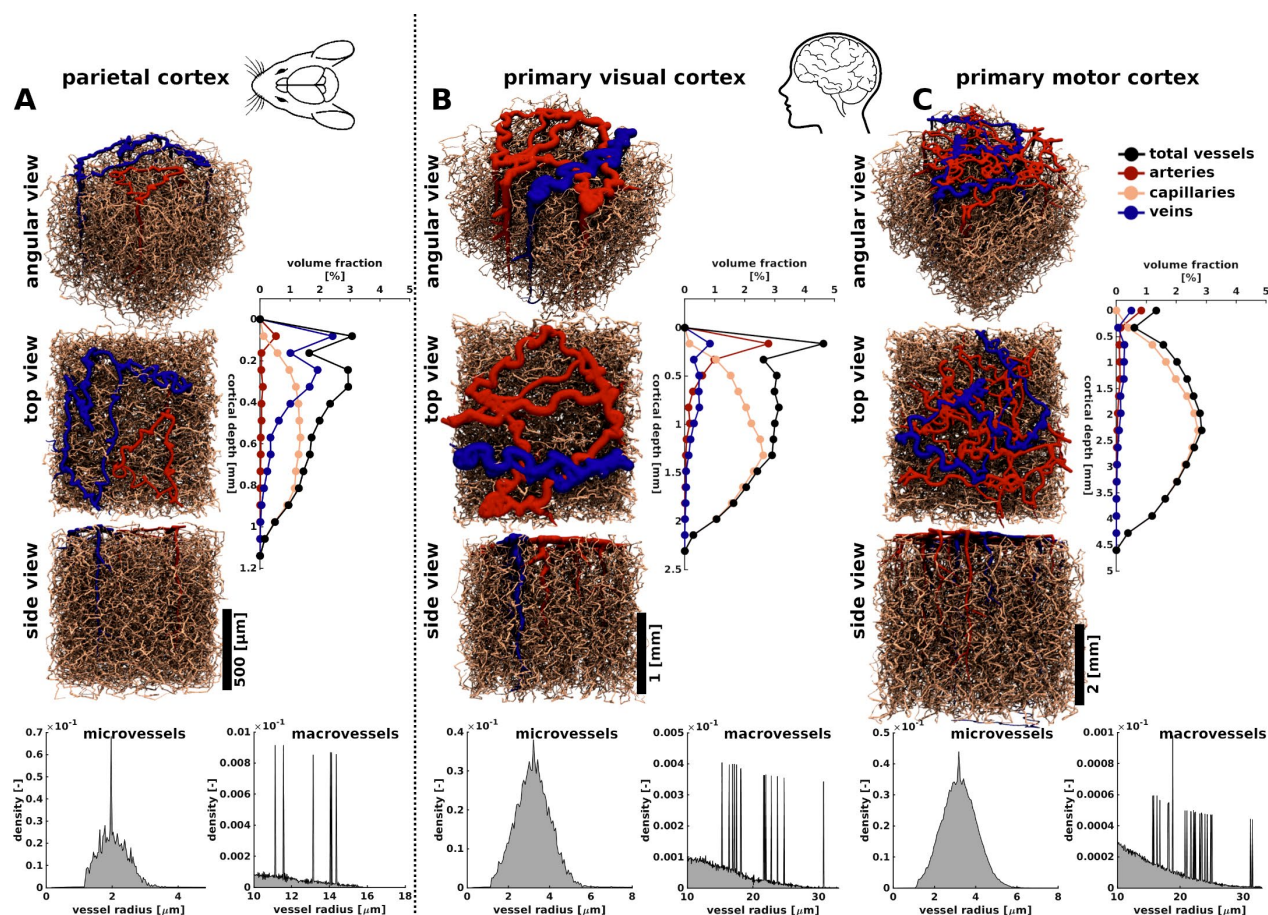
454 In **Figure 1.A**, three different viewing angles of the generated mouse model (angular, top, and  
455 side views) are shown. For the generation of the mouse microvascular compartment, the vessel  
456 radius was set to a mean value of  $2.2 \mu\text{m}$  and a standard deviation of  $0.5 \mu\text{m}$  [Blinder et al., 2013;  
457 Schmid et al., 2019]. The simulated tortuosity was set to 1.2. The vessel distribution across cortical  
458 depth followed a Gaussian distribution with a peak at the middle cortical layers ( $\sim 500 \mu\text{m}$  in depth)  
459 and gradually reduces its value towards the cortical surface and the cortical grey-white matter  
460 boundary. Upon descriptions of the macrovasculature of the mouse, the number of penetrating  
461 arteries and draining veins followed an artery-vein ratio of  $\sim 1:3$  [Blinder et al., 2013; Schmid et al.,  
462 2019]. Hence, two arteries - with radius in the range of  $7 \mu\text{m}$  to  $12 \mu\text{m}$  - and six veins - with radius  
463 in the range of  $10 \mu\text{m}$  to  $14 \mu\text{m}$  - as per  $1.0 \text{ mm}^2$  were used [Blinder et al., 2013; Tsai et al., 2009;  
464 Schmid et al., 2019]. All macrovessels have a cortical penetration labeled as L4, meaning that  
465 approximately all penetrating arteries and draining veins reach a penetration depth of around 70%  
466 to 85% in the model. The distribution of the vessel radius and volume fraction are depicted along  
467 the model.

468 Furthermore, in **Figures 1.B** and **1.C**, two different simulated human cortical regions are shown  
469 in three different viewing angles (angular, top, and side views): a representative primary visual  
470 cortex (**1.B**) and a representative primary motor cortex (**1.C**). The models comprised a  
471 microvascular structure with a vessel radius distribution obtained by a Gaussian distribution with  
472 a mean vessel radius of  $3.235 \mu\text{m}$  and a standard deviation of  $0.85 \mu\text{m}$  [Weber et al., 2008; Cassot  
473 et al., 2009; Lorthois et al., 2011]. The simulated tortuosity was fixed to 1.2. The vessel distribution  
474 across cortical depth followed a Gaussian distribution with a peak at the middle cortical layers  
475 ( $\sim 1.0 \text{ mm}$  and  $2.0 \text{ mm}$ , respectively) and slowly reduces its value towards the cortical surface and  
476 the cortical grey-white matter boundary. The human models were set to an artery-vein ratio of  
477  $\sim 3:1$  [Duvernoy et al., 1981]. For the primary visual cortex, ten arteries -with radius in the range of  
478  $13 \mu\text{m}$  to  $23 \mu\text{m}$ - and four veins -with radius in the range of  $15.65 \mu\text{m}$  to  $31.65 \mu\text{m}$ - as per  $\sim 2.0$



479 mm<sup>2</sup> were set. For the primary motor cortex, twenty arteries and eight veins -with similar vessel  
 480 radius as primary visual cortex- as distributed per ~4.0 mm<sup>2</sup> were implemented [Horton et al.,  
 481 2018; Weber et al., 2008]. Macrovessels were set to different cortical penetrations, labeled from  
 482 L3 to L5 – macrovessels labeled as L5 were connected at the cortical grey-white matter boundary  
 483 and a minimum radial positioning distance between penetrating arteries and draining veins of  
 484 approximately 120 micrometers for both models. The distribution of the vessel radius and volume  
 485 fraction are depicted along the model.

486



487

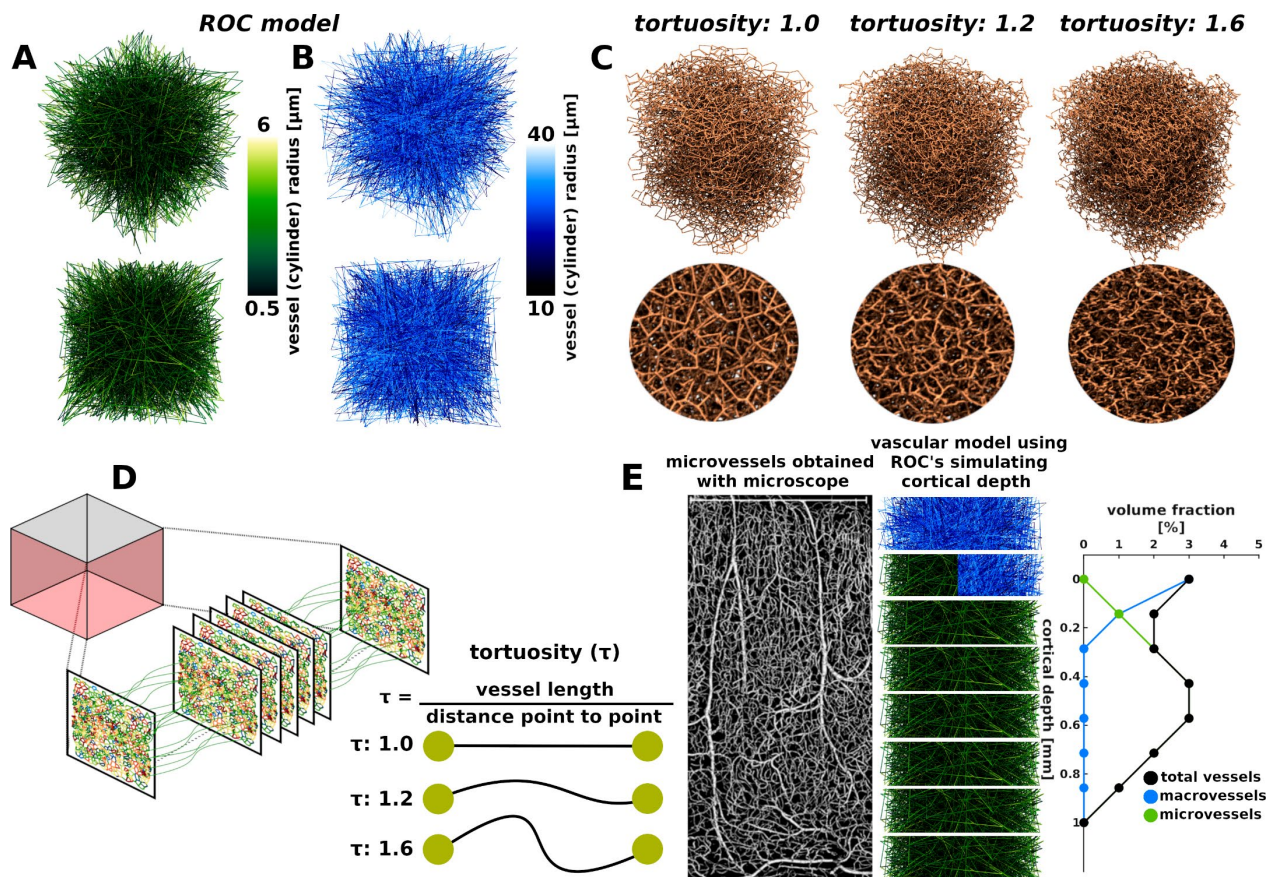
488 **Figure 1.** Comparison of 3D VAMOS representative mouse and human vascular models: (A)  
 489 Representative mouse Model: We utilized the vascular characteristics described by Blinder et al.  
 490 [Blinder et al., 2010] to generate a representative 3D VAMOS model of the parietal cortical  
 491 vessels. Three different angular views (angular, top, and side view) are displayed, along with the  
 492 respective vessel volume fraction across cortical depth. Representative human 3D VAMOS  
 493 models: Taken from literature values [Adams et al., 2015; Weber et al., 2008], we present two  
 494 different cortical regions, the (B) primary visual cortex and (C) primary motor cortex. The vessel

495 volume fraction for each model are displayed along with the vessel radius distribution. Scale bar  
 496 represent a 500  $\mu\text{m}$  (A), 1.0 mm (B) and 2.0 mm (C) cortical depth.

497

498 In **Figure 2**, we present sketches of representative ROC models representing either microvascular  
 499 (**Figure 2.A**; green voxel) or macrovascular (**Figure 2.B**; blue voxel) structures, allowing for a  
 500 visual comparison of their morphology with the respective microvascular network generated by  
 501 the 3D VAMOS algorithm. **Figure 2.C** illustrates different tortuosity level. **Figure 2.D** displays a  
 502 sketch of the generation process of the 3D VAMOS microvascular compartments, as described in  
 503 section 2.1.1. Additionally, to illustrate the difference between realistic 3D vascular networks and  
 504 ROC models, a schematic ROC model is shown in **Figure 2.E**, simulating different vessel radius  
 505 and volume fraction compositions.

506



507

508 **Figure 2.** Sketch of a representative randomly oriented cylinders (ROC) model intended for  
 509 visually comparing the differences in vascular architecture ((A): microvessels; (B): macrovessels)  
 510 and a more realistic microvascular model such as the 3D VAMOS. (C) Examples of representative

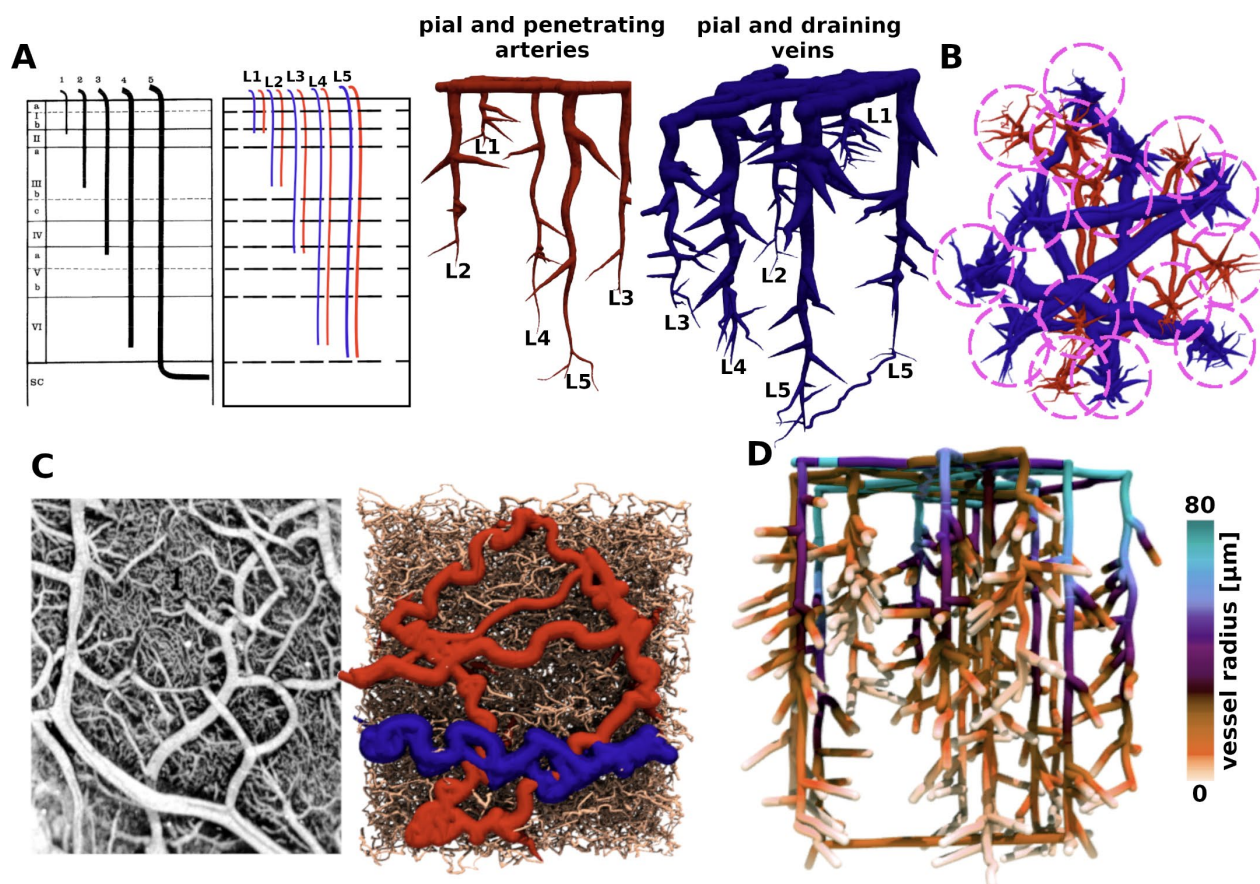
511 *3D VAMOS microvascular architectures for different vessel tortuosity levels. The circular images*  
512 *provide a zoomed-in view of each respective model. A vessel tortuosity with a value of 1.0*  
513 *represents a straight line of edges as computed by the Voronoi tessellation. Tortuosity values*  
514 *larger than 1.0 are simulated using the kernel functions described in section 2.1.1. The model*  
515 *labeled as 1.6 presents a more convoluted or deformed line, resulting in a more realistic vessel*  
516 *topology. (D) Sketch of the generation of the microvascular structure as described in section 2.1.1.*  
517 *The slabs are tiled using a Voronoi tessellation algorithm and then connected to generate a fully*  
518 *interconnected network. (E) A schematic ROC model is shown using different vessel radius and*  
519 *volume fraction compositions in order to simulate cortical thickness along with a microvessel*  
520 *microscopy image.*

521

522 In **Figure 3**, we illustrate the features and capabilities of the 3D VAMOS in generating the  
523 macrovascular architecture. **Figure 3.A** shows the different vessel cortical penetration depth for  
524 both penetrating arteries and draining veins, respectively. The vessel penetration depth follows  
525 the description reported by Duvernoy et al [Duvernoy et al., 1981]. **Figure 3.B** shows the radially  
526 growing of the sub-branches for all the macrovascular architecture. In **Figure 3.C** we qualitatively  
527 demonstrate the resemblance of the cortical pial vessel acquired with microscopic data (left image)  
528 and the 3D VAMOS model (right image). Finally, **Figure 3.D** illustrates the radius distribution,  
529 defined by the Murray's law, for all the macrovascular compartment.

530





531

532 **Figure 3.** Main features accounted on the macrovascular generation. (A) Right: Representation  
 533 of pial and penetrating arteries and pial and draining veins generated with the 3D VAMOS  
 534 algorithm for different cortical penetration depths –from L1 to L5- as described by histological  
 535 characteristics. The left image is adapted from [Duvernoy et al., 1981]. (B) Schematic  
 536 representation of the radial growing of the sub-branches for each of the penetrating arteries and  
 537 draining veins. (C) Visual comparison of a top view from the pial vasculature between the human  
 538 vascular microscopy data [taken from Duvernoy et al., 1981] and the human 3D VAMOS model.  
 539 (D) Representative macrovascular architecture showing the vessel radius distribution according  
 540 to Murray's law ( $R^k_{parent} = R^k_{daughter1} + R^k_{daughter2}$  with  $k = 2$ ).

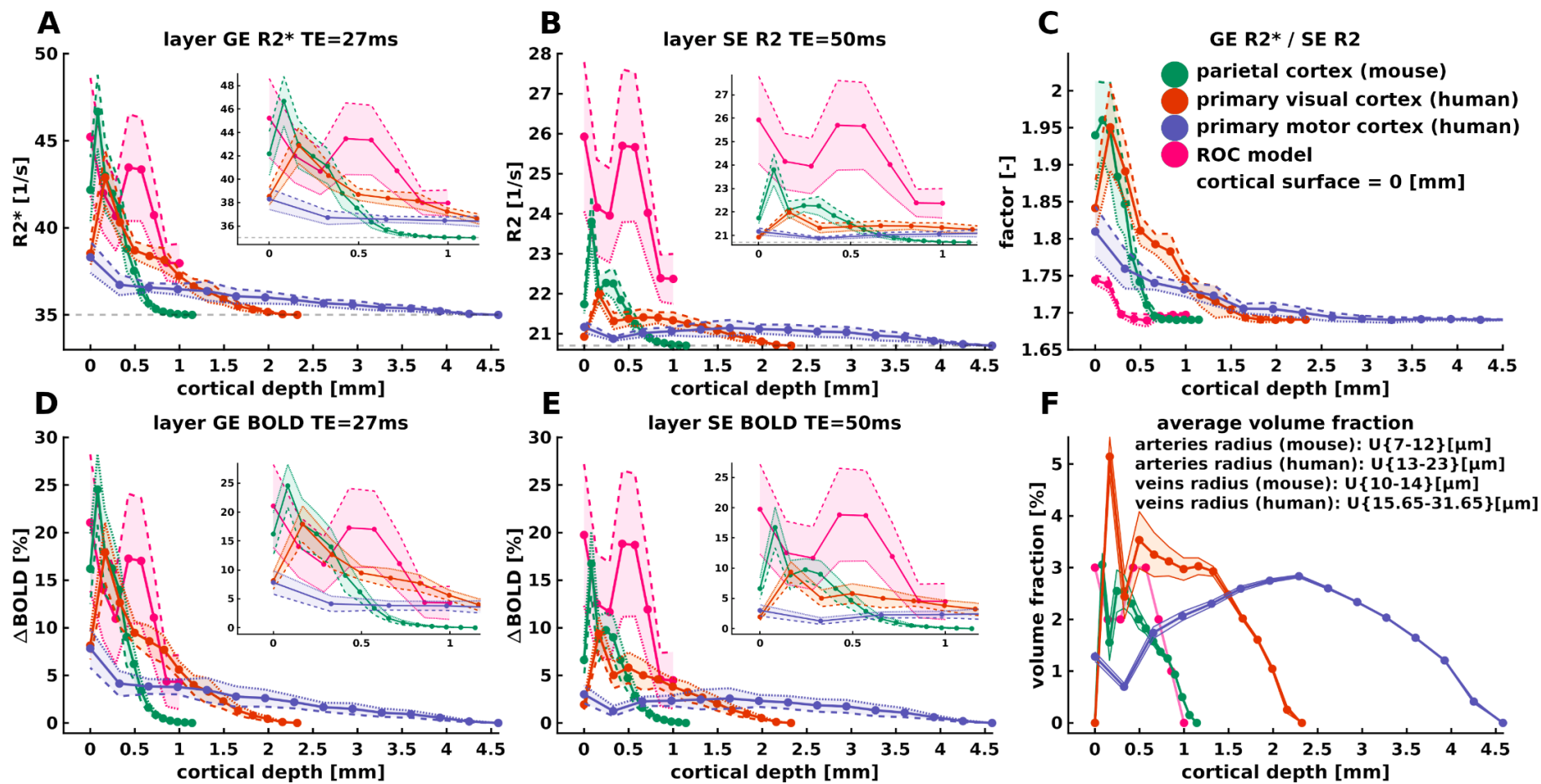
541

542 In **Figure 4**, we present a comparison of layer BOLD signal profiles across species (mouse and  
 543 human) and cortical regions using distinct simulated vascular architecture characteristics,  
 544 including a layer ROC model. The dotted lines of the layer-signal profiles represent the mean  
 545 value and the shaded area represents the standard deviation computed through the different  
 546 oxygen saturation levels computed by the Monte Carlo approach, as described in Section 2.2.2.1.

547 In **Figure 4.A**, we show the  $R2^*$  [1/s] decay rate induced by each vascular model using an echo  
548 time of 27 ms. The  $R2^*$  values range between ~35-48 [1/s]. All models exhibit a larger contribution  
549 towards the cortical/superficial layer, displaying a decreasing  $R2^*$  decay rate towards the GM-WM  
550 boundary –a value relatively similar to the  $R2^*$  value of tissue at 7 tesla ( $R2^*$  of tissue = ~35 [1/s]).  
551 Given that the composition of the superficial vessels in the mouse model is largely comprised of  
552 veins, the mouse model shows a larger  $R2^*$  towards the cortical surface compared to both human  
553 models. The ROC model displays similar  $R2^*$  values compared to the 3D VAMOS models, except  
554 for the increased bump at the middle part of the model due to the larger volume fraction of  
555 microvessels used in the simulation - ROC volume fraction is displayed in **Figure 2**.

556 In **Figure 4.B**, the  $R2$  [1/s] decay rate obtained by a SE readout at an echo time of 50 ms is shown.  
557 The  $R2$  values range between ~20-28 [1/s]. Similar behavior of layer profiles is obtained as  
558 compared to  $R2^*$  decay rates. **Figure 4.C** presents the ratio of the GE  $R2^*$ /SE  $R2$  as a surrogate  
559 measurement of vessel specificity. **Figures 4.D** and **4.E** show the layer BOLD signal changes in  
560 percentage [%]. The GE BOLD signal changes range between ~2%-30% depending on cortical  
561 depth, whereas in the SE BOLD range within an interval of ~1% to 20% depending on cortical  
562 depth. GE BOLD signal change shows a larger contribution at the cortical surface, reducing its  
563 value across cortical depth. Similarly, SE BOLD signal changes present larger values at the  
564 cortical surface, reducing across cortical depth, except that these values are smaller compared to  
565 the GE BOLD signal changes. Finally, in **Figure 4.F**, we plot the average volume fraction that  
566 iteratively changes the morphology of each vascular model while conserving the same topological  
567 features.

568



569

570 **Figure 4.** Comparison of layer BOLD signal profiles across species (mouse and human) and cortical regions using distinct simulated  
 571 vascular architecture characteristics including a layer ROC model as defined in **Figure 2.** (continues...)

572 *(continues...)*. Dotted lines represent the mean value computed through the different Monte Carlo  
573 simulations, while the shaded area represents the standard deviation – dashed lines represent  
574 the lowest oxygen saturation value, while the segmented line represents the highest oxygen  
575 saturation value. **(A)** and **(B)** depict the  $R2^*$  decay rate across cortical depth, respectively. **(C)**  
576 shows the  $GER2^*/SER2$  ratio as a surrogate measurement of vessel specificity. **(D)** and **(E)**  
577 present the layer BOLD signal changes across cortical depth for GE and SE, respectively; and **(F)**  
578 the average volume fraction obtained through the Monte Carlo repetitions. In mouse, the vascular  
579 architecture features a cortical depth of approximately  $1.0\text{ mm}^3$ , with an artery-vein ratio of 1:3 (2  
580 arteries -with radius in the range of 7 to 12  $\mu\text{m}$ - and 6 veins -with radius in the range of 10 to 14  
581  $\mu\text{m}$ -per  $1\text{ mm}^2$ ), and microvessel radius parameters of mean =  $2\ \mu\text{m}$  and std =  $0.5\ \mu\text{m}$ . Human  
582 primary visual cortex simulations depict a cortical depth of around  $2.0\text{ mm}^3$ , with an artery-vein  
583 ratio of 3:1 (10 arteries -with radius in the range of 13 to 23  $\mu\text{m}$ - and 4 veins -with radius in the  
584 range of 15.65 to 31.65  $\mu\text{m}$ - per  $\sim 2.0\text{ mm}^2$ ), and microvessel radius parameters of mean =  $3.235\ \mu\text{m}$   
585 and std =  $0.85\ \mu\text{m}$ . Similarly, the simulated vascular architecture of the human primary motor  
586 cortex includes a cortical depth of approximately  $4.0\text{ mm}^3$ , an artery-vein ratio of 3:1 (20 arteries  
587 and 8 veins -with similar vessel radius as visual cortex- per  $\sim 4.0\text{ mm}^2$ ), and microvessel radius  
588 parameters of mean =  $3.235\ \mu\text{m}$  and std =  $0.85\ \mu\text{m}$ . Oxygen saturation levels are described in  
589 section 2.2.2.

590

## 591 **4. DISCUSSION**

### 592 **4.1 General discussion**

593 In order to understand the functional MRI signals obtained at high spatial resolution, i.e. at  
594 submillimeter scales, we have developed a computational framework reflecting a fully synthetic  
595 human 3D cortical vascular model obeying the MR physics governing the MR signal formation  
596 process.

597 The so-called 3D VAMOS algorithm generates both microvascular and macrovascular  
598 angioarchitectures defined by histological, morphological and topological features obtained from  
599 the human cortical vasculature. The microvasculature is generated through Voronoi tessellation  
600 and kernel functions, while the macrovasculature is generated by kernel functions. Both vessel  
601 compartments depend on statistical properties taken from literature values.

602 The computational time required to generate both macrovasculature and microvasculature  
603 depends on cortical dimensions and characteristics. Microvasculature is typically generated within

604 seconds to a couple of minutes, while macrovasculature is generated in less than ~2 seconds.  
605 Other computational algorithms that resemble realistic vascular architecture [[Hartung et al, 2021](#)],  
606 using a different mathematical approach, can take several days of computation, depending on  
607 vascular architecture properties and vessel characteristics. The proposed 3D VAMOS offers the  
608 advantage of relatively fast generation of representative vascular angioarchitecture. This allows  
609 for increased statistical power/ averaging of the BOLD signals, as each MR signal iteration creates  
610 a new vascular morphology while maintaining vascular topology features – similar to averaging  
611 voxels in data analysis pipelines.

612 Further, after generating both vascular compartments, the VAMOS algorithm results in a fully  
613 interconnected network. This crucial feature will enable an easily extension to include  
614 hemodynamic simulations with manipulation of the boundary conditions at the blood inlets/outlets  
615 sources, such as pial arteries and veins, respectively, and vasodilation changes of specific vessels  
616 or vascular compartments [[Lorthois et al., 2011](#)]. This ability is a significant improvement  
617 compared to the SVM [[Báez-Yáñez et al., 2023](#)], where the macrovascular compartment was  
618 merely superimposed on the microvasculature without being connected to it.

619 Nevertheless, the 3D VAMOS model enables simulation of specific oxygen saturation states per  
620 vascular compartment and biophysical interactions, such as diffusion effects of water in tissue, to  
621 characterize the intravascular and extravascular signal contribution of diverse vascular  
622 architectures to the gradient-echo (GE) BOLD and spin-echo (SE) BOLD signals, either at the  
623 voxel level acquired at high spatial resolutions or across cortical depth.

624

#### 625 **4.2 On the fully synthetic human 3D VAMOS model**

626 One of the motivations for developing a fully synthetic 3D vascular model is the limitation of human  
627 cortical vasculature samples. Currently, 3D visualization of ex-vivo human vascular network  
628 samples can be achieved using immunohistochemistry labeling combined with microscopy or x-  
629 ray microtomography imaging techniques. However, these technologies are still being developed  
630 and are challenging to apply, especially for sufficiently large tissue samples. Moreover, the tissue  
631 samples may suffer from degradation and deformation. As a result, acquiring large volumes of  
632 human cortical vasculature (>1 mm<sup>3</sup> isotropic) is quite difficult [[Cassot et al., 2006](#); [Lauwers et al.,](#)  
633 [2008](#); [Duvernoy et al., 1981](#)]. To overcome the limitations of a realistic 3D representation of the  
634 human cortical vasculature, the 3D VAMOS computational approach provides a versatile solution



635 by generating human vascular models based on angioarchitectural characteristics derived from  
636 literature values.

637 Structurally, the ROC models prove inadequate in representing vascular networks when  
638 attempting to understand the formation of the BOLD signal at high spatial resolutions (see **Figure**  
639 **2** and **Figure 4**). It has been demonstrated that at mesoscopic levels, the angioarchitecture  
640 adheres to well-defined patterns, such as the mesh-like network of the capillary bed. While it is  
641 indeed possible to generate ROC models by assuming monosized cylinders or a mixture of  
642 cylinder sizes within a volumetric space while maintaining the volume fraction, such vascular  
643 models cannot effectively compute specific vascular topologies, such as the well-structured  
644 penetrating arteries and draining veins [Markuerkiaga et al., 2016]. Furthermore, conducting  
645 hemodynamic simulations becomes more complex due to the high dependence of hemodynamic  
646 changes on vascular properties and topology.

647 Further, a detailed model of the cerebral vasculature, such as the 3D VAMOS model, is necessary  
648 to understand the underlying principles of tissue perfusion at submillimeter spatial scales. The 3D  
649 VAMOS model could be used to further our understanding of physiology. For instance, it can  
650 provide insights into the spatial distribution of oxygen by the vascular network and other  
651 hemodynamic information at any specific point within the neural tissue supplied by the vascular  
652 network [Risser et al, 2007].

653 Lauwers et al [Lauwers et al, 2008] observed that large vessels (macro vessels) contribute more  
654 to the vascular volume in the upper layers of the cortex, while the capillary compartment made a  
655 greater contribution in the middle third of the cortex. This cortical vascular feature can be well  
656 captured by the 3D VAMOS, as observed in the cortical depth profiles in **Figure 1**, given that the  
657 definition of the vessel decreasing vessel radius across cortical depth using the kernel functions.  
658 This distribution pattern could potentially influence the layer profiles of functional activity that have  
659 recently been observed at high resolution layer fMRI, and thus, the 3D VAMOS model is suited to  
660 investigate further the layer-specificity of this functional signal [Markuerkiaga et al., 2021; Bause  
661 et al., 2020]. Moreover, pial arteries are known to exhibit anastomoses to efficiently support  
662 regions of high perfusion demand or collateral flow [Adams et al., 2015]. However, in this  
663 manuscript, anastomoses are not implemented. Only main pial vessel segments belonging to the  
664 large feeding arteries are included. Pial veins do not exhibit anastomoses at any cortical depth  
665 level [Duvernoy et al., 1981].

666 It is important to note the flexibility that the 3D VAMOS offers. For example, the representative  
667 vascular models for any specific brain region are not constrained to specific macro vessel

668 topological or morphological features. It can generate different realistic or, even, non-realistic  
669 artery-vein ratios to understand the impact of the macrovasculature on hemodynamic changes  
670 and its direct effect on BOLD fMRI signal formation.

671 Another advantage of the 3D VAMOS is that the vascular network is fully connected. This will  
672 allow for local hemodynamic simulations of changes in CBF, CBV, and corresponding oxygen  
673 saturation levels [Báez-Yáñez et al., 2023]. This capability can help understand the specific  
674 physiological roles of the vascular compartments, their contributions to hemodynamic changes  
675 and the direct impact on the BOLD signal. For example, given its fully vascular connectivity, in  
676 future studies, we envision investigating the local transients of red blood cells in a vascular network  
677 and their effects on the heterogeneity of mean transit time [Jespersen et al., 2012], among other  
678 hemodynamic changes induced by neuronal activation or other kind of stimuli, such as controlled  
679 gas-challenges.

680

#### 681 **4.3 On the fully synthetic mouse 3D VAMOS model**

682 Another motivation for developing a fully synthetic 3D vascular model is the limitation faced by  
683 advanced imaging techniques, such as two-photon microscopy or scanning electron microscopy,  
684 in capturing detailed mouse vascular structures due to the finite penetration capacity of the  
685 illumination they employ. Consequently, the depth of field of view in these methods is typically  
686 restricted to a few hundred micrometers at best. The 3D VAMOS approach helps to understand  
687 the BOLD signal formation and effects of the vascular topology and hemodynamics at the level of  
688 MRI voxels, as those acquired in fMRI measurements even at the mesoscopic laminar level.

689 Moreover, microscopy imaging data, such as two-photon microscopy, typically depict biological  
690 vascular structures that exhibit irregular vessel shapes. Image noise and visualization artifacts  
691 further contribute to vessel characterization degradation. Any disturbances can significantly  
692 impact the skeletonization process, often resulting in undesirable outcomes. Skeletonization is  
693 inherently sensitive to these minor boundary perturbations, necessitating the removal of unwanted  
694 effects in a post-processing stage. Distinguishing between genuine features and artifacts is often  
695 challenging, making segmentation a potential source of error in topological descriptions. The 3D  
696 VAMOS can help overcome this limitation by providing versatility in generating different vascular  
697 approximations for a wide range of vascular parameters at low computational cost and time – the  
698 generation of a fully connected vascular network can take less than ~45 seconds, depending on  
699 the simulated vascular features and desired volumetric space. Nevertheless, refinement in post-

700 processing microscopy data will enhance our understanding of such complex networks and  
701 provide a better-informed 3D VAMOS vascular network.

702

#### 703 **4.4 On the simulated BOLD fMRI signals**

704 Given that the main vascular contribution to BOLD signal formation is attributed to the venous  
705 compartment, the mouse model exhibits larger decay rates and BOLD signal changes near the  
706 cortical surface compared to the human models –due to the artery/vein ratio. This highlights the  
707 importance of employing vascular models that replicate specific vascular features found in  
708 different species in order to reduce misinterpretations of the measured BOLD fMRI data across  
709 species.

710 The primary motor cortex, with an average thickness of roughly 4.0 mm in humans, presents a  
711 notable contrast to the primary visual cortex, which averages around ~2.0 mm [[Palomero-  
712 Gallagher et al, 2019](#)]. This distinction holds significance when applying imaging and analysis  
713 methods from one regional cortex to another. Despite achieving equivalent imaging resolution in  
714 both areas, the primary motor cortex exhibits lower relative signal changes (see **Figure 4**). Hence,  
715 when comparing layer activity profiles across participants and brain regions, it is important to  
716 consider their relative cortical thickness.

717 For all models, GE R2\* decay rates increase towards the cortical pial surface. SE R2 decay rates  
718 also increase towards the cortical pial surface, though to a lesser extent due to the refocusing  
719 180-degree pulse. Despite this pulse, the influence of macrovessels at the cortical pial surface  
720 remains significant depending on the simulated oxygen saturation level. In the deeper layers, most  
721 contributions to GE R2\* and SE R2 originate from the tissue's R2\*, with a small weighted  
722 contribution from extravascular and intravascular CBV and minor contributions from R2'.

723 Our findings suggest that the diverse vascular architecture in deeper gray matter has a diminished  
724 effect on the laminar signatures of both BOLD signal changes and R2\* decay rates (see **Figure  
725 4**). Conversely, superficial layers (pial surface) exhibit significant differences in the topology of  
726 large vessels, leading to a less uniform BOLD signal change in these layers. These simulation  
727 results highlight the necessity of addressing the bias of large vessels toward the pial surface in  
728 laminar fMRI data through filtering and/or normalization techniques [[Vizioli et al., 2021](#)].

729

730

#### 731 **4.5 Future studies and computational improvements**

732 Current noninvasive functional neuroimaging methods mainly rely on detecting the hemodynamic  
733 response to neuronal activation. Improving our understanding of cortical vascular topology and  
734 functioning will enhance our insights into the effects of local cerebral blood flow disruptions on  
735 both local and global perfusions. Thus, dynamic changes of cerebral blood volume and flow will  
736 be included in future studies in order to understand the dynamic processes that drives the  
737 hemodynamic fingerprint of the BOLD signal formation and other neuroimaging techniques, such  
738 as perfusion imaging.

739 To enhance confidence in the resemblance of the 3D VAMOS model to realistic human vascular  
740 angioarchitecture, we intend to compare our model to various quantitative measurements in future  
741 studies. These may include distance map values of the tissue-vessel spatial distribution. Another  
742 example could be the analysis of the vascular surface-to-volume ratio.

743 Another methodological improvement that we will consider in the near future is the generation of  
744 vascular angioarchitecture that presents a certain degree of simulated cortical curvature. Ongoing  
745 developments include the 2D slabs, used to create the Voronoi tessellation, to be inserted in quasi-  
746 spherical spaces. The 2D slabs could be placed radially - with respect to a certain origin point to  
747 manipulate the degree of “orthogonality” with respect to the cortical surface.

748 In addition to this, we have assumed isotropic diffusion motion within the tissues. It has been  
749 shown that different diffusion regimes can have a strong effect on the BOLD signal, such as the  
750 one provided by the CSF [[van Horen et al., 2023](#)]. In future studies, we plan to implement a  
751 diffusion coefficient value dependent on cortical depth, i.e., CSF water motion in the superficial  
752 layers displaying a slightly different value compared to the deeper layers.

753 Moreover, it has been observed that penetrating arteries in certain cortical regions create  
754 cylindrical spaces devoid of capillaries in their proximity [[Duvernoy et al., 1981](#); [Cassot et al., 2010](#);  
755 [Lauwers et al., 2008](#)]. We plan to incorporate this realistic topological characteristic into the  
756 generation of the microvascular network in the 3D VAMOS model.

757

#### 758 **5. CONCLUSION**

759 Understanding the spatial specificity of hemodynamic fingerprint BOLD fMRI signals acquired at  
760 mesoscale through a more robust and complex modeling approach, such as the one presented in  
761 the 3D VAMOS computational approach, will enhance our understanding of neuroimaging at

762 submillimeter scales, both in healthy and pathological conditions. Therefore, the 3D VAMOS  
763 computational approach will help understand the influence of human 3D vascular architectures on  
764 the formation of hemodynamic fingerprint GE BOLD and SE BOLD signals across cortical depth  
765 and/or voxel-wise levels at high spatial imaging resolutions, as well as the impact of pulse  
766 sequence parameters on BOLD signal changes in submillimeter MRI acquisitions.

767

#### 768 **ACKNOWLEDGEMENTS (54 words)**

769 This work was supported by the National Institute of Mental Health of the National Institutes of  
770 Health under the Award Number R01MH111417 and the Dutch Research Council under award  
771 number 18969. The content is solely the responsibility of the authors and does not necessarily  
772 represent the official views of the National Institutes of Health.

773

#### 774 **AUTHOR CONTRIBUTION STATEMENT**

775 Conceptualization: MGBY, WS, AAB, JCWS, NP.

776 3D VAMOS computational pipeline – including MR signals: MGBY.

777 BOLD fMRI experiments: WS, AAB, ECAR.

778 BOLD fMRI data analysis: WS, AAB, ECAR.

779 Figures design: MGBY.

780 Writing - original draft: MGBY.

781 Writing – review and editing: All authors.

782 Funding acquisition: MvO and NP.

783

#### 784 **DISCLOSURE/CONFLICT OF INTEREST**

785 The authors declare that they have no known competing financial interests, conflict of interest or  
786 personal relationships that could have appeared to influence the work reported in this paper.

787

788

789 **CODE/DATA AVAILABILITY STATEMENT**

790 The code and data underlying the findings of this study are available from the corresponding  
791 author upon request. Access is subject to a nonexclusive, revocable, non-transferable, and limited  
792 right to use solely for research and evaluation purposes, excluding any commercial use.

793

794 **REFERENCES**

- 795 1. Adams DL, Piserchia V, Economides JR, Horton JC. Vascular Supply of the Cerebral Cortex  
796 is Specialized for Cell Layers but Not Columns. *Cereb Cortex*. 2015 Oct;25(10):3673-81. doi:  
797 10.1093/cercor/bhu221. Epub 2014 Sep 21. PMID: 25246513; PMCID: PMC4585511.
- 798 2. Báez-Yáñez M.G., Siero JCW, Petridou N. A mechanistic computational framework to  
799 investigate the hemodynamic fingerprint of the blood oxygenation level-dependent signal.  
800 *NMR Biomed*. 2023 Aug 29: e5026
- 801 3. Báez-Yáñez MG, Ehses P, Mirkes C, Tsai PS, Kleinfeld D, Scheffler K. The impact of vessel  
802 size, orientation and intravascular contribution on the neurovascular fingerprint of BOLD  
803 bSSFP fMRI. *Neuroimage*. 2017 Dec; 163:13-23. doi: 10.1016/j.neuroimage.2017.09.015.  
804 Epub 2017 Sep 8. PMID: 28890417; PMCID: PMC5857886.
- 805 4. Bandettini PA, Kwong KK, Davis TL, Tootell RB, Wong EC, Fox PT, Belliveau JW, Weisskoff  
806 RM, Rosen BR. Characterization of cerebral blood oxygenation and flow changes during  
807 prolonged brain activation. *Hum Brain Mapp*. 1997;5(2):93-109. PMID: 10096414.
- 808 5. Bandettini PA, Wong EC, Jesmanowicz A, Hinks RS, Hyde JS. Spin-echo and gradient-echo  
809 EPI of human brain activation using BOLD contrast: a comparative study at 1.5 T. *NMR*  
810 *Biomed*. 1994 Mar;7(1-2):12-20. doi: 10.1002/nbm.1940070104. PMID: 8068520.
- 811 6. Bause J, Polimeni JR, Stelzer J, In MH, Ehses P, Kraemer-Fernandez P, Aghaeifar A, Lacosse  
812 E, Pohmann R, Scheffler K. Impact of prospective motion correction, distortion correction  
813 methods and large vein bias on the spatial accuracy of cortical laminar fMRI at 9.4 Tesla.  
814 *Neuroimage*. 2020 Mar; 208:116434. doi: 10.1016/j.neuroimage.2019.116434. Epub 2019  
815 Dec 6. PMID: 31812715.
- 816 7. Belliveau JW, Rosen BR, Kantor HL, Rzedzian RR, Kennedy DN, McKinstry RC, Vevea JM,  
817 Cohen MS, Pykett IL, Brady TJ. Functional cerebral imaging by susceptibility-contrast NMR.  
818 *Magn Reson Med*. 1990 Jun;14(3):538-46. doi: 10.1002/mrm.1910140311. PMID: 2355835.
- 819 8. Bieri O, Scheffler K. Effect of diffusion in inhomogeneous magnetic fields on balanced steady-  
820 state free precession. *NMR Biomed*. 2007 Feb;20(1):1-10. doi: 10.1002/nbm.1079. PMID:  
821 16947639.



- 822 9. Blinder P, Shih AY, Rafie C, Kleinfeld D. Topological basis for the robust distribution of blood  
823 to rodent neocortex. *Proc Natl Acad Sci U S A*. 2010 Jul 13;107(28):12670-5. doi:  
824 10.1073/pnas.1007239107. Epub 2010 Jun 28. PMID: 20616030; PMCID: PMC2906564.
- 825 10. Blinder P, Tsai PS, Kaufhold JP, Knutsen PM, Suhl H, Kleinfeld D. The cortical angiome: an  
826 interconnected vascular network with noncolumnar patterns of blood flow. *Nat Neurosci*. 2013  
827 Jul;16(7):889-97. doi: 10.1038/nn.3426. Epub 2013 Jun 9. PMID: 23749145; PMCID:  
828 PMC4141079.
- 829 11. Boxerman JL, Hamberg LM, Rosen BR, Weisskoff RM. MR contrast due to intravascular  
830 magnetic susceptibility perturbations. *Magn Reson Med*. 1995 Oct;34(4):555-66. doi:  
831 10.1002/mrm.1910340412. PMID: 8524024.
- 832 12. Butman JA, Floeter MK. Decreased thickness of primary motor cortex in primary lateral  
833 sclerosis. *AJNR Am J Neuroradiol*. 2007 Jan;28(1):87-91. PMID: 17213431; PMCID:  
834 PMC8134097.
- 835 13. Cassot F, Lauwers F, Lorthois S, Puwanarajah P, Cances-Lauwers V, Duvernoy H. Branching  
836 patterns for arterioles and venules of the human cerebral cortex. *Brain Res*. 2010 Feb  
837 8;1313:62-78. doi: 10.1016/j.brainres.2009.12.007. Epub 2009 Dec 11. PMID: 20005216.
- 838 14. Cassot F, Lauwers F, Lorthois S, Puwanarajah P, Duvernoy H. Scaling laws for branching  
839 vessels of human cerebral cortex. *Microcirculation*. 2009 May;16(4):331-44, 2 p following 344.  
840 doi: 10.1080/10739680802662607. PMID: 19301179.
- 841 15. Chausse, Jacob, Avery JL Berman, and J. Jean Chen. "BOLDswimsuite: A new software suite  
842 for forward modeling of the BOLD fMRI signal." *bioRxiv* (2024): 2024-01.
- 843 16. Choi S, Zeng H, Chen Y, Sobczak F, Qian C, Yu X. Lamina-specific functional connectivity  
844 mapping with multi-slice line-scanning fMRI. *Cereb Cortex*. 2022 Oct 8;32(20):4492-4501. doi:  
845 10.1093/cercor/bhab497. Erratum in: *Cereb Cortex*. 2023 Mar 21;33(7):4188. PMID:  
846 35107125; PMCID: PMC9574235.
- 847 17. De Martino F, Zimmermann J, Muckli L, Ugurbil K, Yacoub E, Goebel R. Cortical depth  
848 dependent functional responses in humans at 7T: improved specificity with 3D GRASE. *PLoS*  
849 *One*. 2013;8(3):e60514. doi: 10.1371/journal.pone.0060514. Epub 2013 Mar 22. PMID:  
850 23533682; PMCID: PMC3606277.
- 851 18. Dumoulin SO, Fracasso A, van der Zwaag W, Siero JCW, Petridou N. Ultra-high field MRI:  
852 Advancing systems neuroscience towards mesoscopic human brain function. *Neuroimage*.  
853 2018 Mar; 168:345-357. doi: 10.1016/j.neuroimage.2017.01.028. Epub 2017 Jan 16. PMID:  
854 28093360.
- 855 19. Dumoulin SO. Layers of Neuroscience. *Neuron*. 2017 Dec 20;96(6):1205-1206. doi:  
856 10.1016/j.neuron.2017.12.004. PMID: 29268088.

- 857 20. Duvernoy HM, Delon S, Vannson JL. Cortical blood vessels of the human brain. *Brain Res*  
858 *Bull.* 1981 Nov ;7(5):519-79. doi: 10.1016/0361-9230(81)90007-1. PMID : 7317796.
- 859 21. El-Bouri WK, Payne SJ. Multi-scale homogenization of blood flow in 3-dimensional human  
860 cerebral microvascular networks. *J Theor Biol.* 2015 Sep 7;380:40-7. doi:  
861 10.1016/j.jtbi.2015.05.011. Epub 2015 May 15. PMID: 25986433.
- 862 22. Fischl B, Dale AM. Measuring the thickness of the human cerebral cortex from magnetic  
863 resonance images. *Proceedings of the National Academy of Sciences.* 2000 Sep  
864 26;97(20):11050-5.
- 865 23. Fracasso A, Luijten PR, Dumoulin SO, Petridou N. Laminar imaging of positive and negative  
866 BOLD in human visual cortex at 7T. *Neuroimage.* 2018 Jan 1; 164:100-111. doi:  
867 10.1016/j.neuroimage.2017.02.038. Epub 2017 Feb 14. PMID: 28213112.
- 868 24. Fujita N. Extravascular contribution of blood oxygenation level-dependent signal changes: a  
869 numerical analysis based on a vascular network model. *Magn Reson Med.* 2001  
870 Oct;46(4):723-34. doi: 10.1002/mrm.1251. PMID: 11590649.
- 871 25. Gagnon L, Sakadžić S, Lesage F, Musacchia JJ, Lefebvre J, Fang Q, Yücel MA, Evans KC,  
872 Mandeville ET, Cohen-Adad J, Polimeni JR, Yaseen MA, Lo EH, Greve DN, Buxton RB, Dale  
873 AM, Devor A, Boas DA. Quantifying the microvascular origin of BOLD-fMRI from first principles  
874 with two-photon microscopy and an oxygen-sensitive nanoprobe. *J Neurosci.* 2015 Feb  
875 25;35(8):3663-75. doi: 10.1523/JNEUROSCI.3555-14.2015. PMID: 25716864; PMCID:  
876 PMC4339366.
- 877 26. Goense JB, Logothetis NK. Laminar specificity in monkey V1 using high-resolution SE-fMRI.  
878 *Magn Reson Imaging.* 2006 May;24(4):381-92. doi: 10.1016/j.mri.2005.12.032. Epub 2006  
879 Mar 13. PMID: 16677944.
- 880 27. Gould IG, Tsai P, Kleinfeld D, Linninger A. The capillary bed offers the largest hemodynamic  
881 resistance to the cortical blood supply. *J Cereb Blood Flow Metab.* 2017 Jan;37(1):52-68. doi:  
882 10.1177/0271678X16671146. Epub 2016 Oct 10. PMID: 27780904; PMCID: PMC5363755.
- 883 28. Gülban ÖF, Huber R. Computing geometric layers and columns on continuously improving  
884 human (f)MRI data. *Layer fMRI blog* (2024)  
885 <https://layerfmri.com/2024/04/18/layerification/#more-4321>
- 886 29. Han S, Eun S, Cho H, Uludağ K, Kim SG. Improved laminar specificity and sensitivity by  
887 combining SE and GE BOLD signals. *Neuroimage.* 2022 Dec 1; 264:119675. doi:  
888 10.1016/j.neuroimage.2022.119675. Epub 2022 Oct 13. PMID: 36243267.
- 889 30. Hartung G, Badr S, Mihelic S, Dunn A, Cheng X, Kura S, Boas DA, Kleinfeld D, Alaraj A,  
890 Linninger AA. Mathematical synthesis of the cortical circulation for the whole mouse brain-part



- 891 II: Microcirculatory closure. *Microcirculation*. 2021 Jul;28(5):e12687. doi: 10.1111/micc.12687.  
892 Epub 2021 Apr 8. PMID: 33615601; PMCID: PMC8504684.
- 893 31. Hartung G, Vesel C, Morley R, Alaraj A, Sled J, Kleinfeld D, Linninger A. Simulations of blood  
894 as a suspension predicts a depth dependent hematocrit in the circulation throughout the  
895 cerebral cortex. *PLoS Comput Biol*. 2018 Nov 19;14(11):e1006549. doi:  
896 10.1371/journal.pcbi.1006549. PMID: 30452440; PMCID: PMC6277127.
- 897 32. Havlicek M, Ivanov D, Poser BA, Uludag K. Echo-time dependence of the BOLD response  
898 transients - A window into brain functional physiology. *Neuroimage*. 2017 Oct 1; 159:355-370.  
899 doi: 10.1016/j.neuroimage.2017.07.034. Epub 2017 Jul 18. PMID: 28729160.
- 900 33. Hirsch S, Reichold J, Schneider M, Székely G, Weber B. Topology and hemodynamics of the  
901 cortical cerebrovascular system. *J Cereb Blood Flow Metab*. 2012 Jun;32(6):952-67. doi:  
902 10.1038/jcbfm.2012.39. Epub 2012 Apr 4. PMID: 22472613; PMCID: PMC3367227.
- 903 34. Horton JC, Adams DL. Patterns of Cortical Visual Field Defects From Embolic Stroke  
904 Explained by the Anastomotic Organization of Vascular Microlobules. *J Neuroophthalmol*.  
905 2018 Dec;38(4):538-550. doi: 10.1097/WNO.0000000000000733. PMID: 30418333; PMCID:  
906 PMC6913876.
- 907 35. Huber L, Handwerker DA, Jangraw DC, Chen G, Hall A, Stüber C, Gonzalez-Castillo J, Ivanov  
908 D, Marrett S, Guidi M, Goense J, Poser BA, Bandettini PA. High-Resolution CBV-fMRI Allows  
909 Mapping of Laminar Activity and Connectivity of Cortical Input and Output in Human M1.  
910 *Neuron*. 2017 Dec 20;96(6):1253-1263.e7. doi: 10.1016/j.neuron.2017.11.005. Epub 2017  
911 Dec 7. PMID: 29224727; PMCID: PMC5739950.
- 912 36. Jespersen SN, Østergaard L. The roles of cerebral blood flow, capillary transit time  
913 heterogeneity, and oxygen tension in brain oxygenation and metabolism. *J Cereb Blood Flow*  
914 *Metab*. 2012 Feb;32(2):264-77. doi: 10.1038/jcbfm.2011.153. Epub 2011 Nov 2. PMID:  
915 22044867; PMCID: PMC3272609.
- 916 37. Kashyap S, Ivanov D, Havlicek M, Poser BA, Uludağ K. Impact of acquisition and analysis  
917 strategies on cortical depth-dependent fMRI. *Neuroimage*. 2018 Mar; 168:332-344. doi:  
918 10.1016/j.neuroimage.2017.05.022. Epub 2017 May 12. PMID: 28506874.
- 919 38. Keller AL, Schüz A, Logothetis NK, Weber B. Vascularization of cytochrome oxidase-rich blobs  
920 in the primary visual cortex of squirrel and macaque monkeys. *J Neurosci*. 2011 Jan  
921 26;31(4):1246-53. doi: 10.1523/JNEUROSCI.2765-10.2011. PMID: 21273409; PMCID:  
922 PMC6623626.
- 923 39. Khajehim M, Nasiraei Moghaddam A. Investigating the spatial specificity of S2-SSFP fMRI: A  
924 Monte Carlo simulation approach. *Magn Reson Imaging*. 2017 Apr; 37:282-289. doi:  
925 10.1016/j.mri.2016.11.016. Epub 2016 Nov 24. PMID: 27890778.

- 926 40. Kiselev VG, Novikov DS. Transverse NMR relaxation in biological tissues. *Neuroimage*. 2018  
927 Nov 15; 182:149-168. doi: 10.1016/j.neuroimage.2018.06.002. Epub 2018 Jun 7. PMID:  
928 29885485; PMCID: PMC6175675.
- 929 41. Kiselev VG, Posse S. Analytical model of susceptibility-induced MR signal dephasing: effect  
930 of diffusion in a microvascular network. *Magn Reson Med*. 1999 Mar;41(3):499-509. doi:  
931 10.1002/(sici)1522-2594(199903)41:3<499:aid-mrm12>3.0.co;2-o. PMID: 10204873.
- 932 42. Kiselev VG. On the theoretical basis of perfusion measurements by dynamic susceptibility  
933 contrast MRI. *Magn Reson Med*. 2001 Dec;46(6):1113-22. doi: 10.1002/mrm.1307. PMID:  
934 11746577.
- 935 43. Lauwers F, Cassot F, Lauwers-Cances V, Puwanarajah P, Duvernoy H. Morphometry of the  
936 human cerebral cortex microcirculation: general characteristics and space-related profiles.  
937 *Neuroimage*. 2008 Feb 1;39(3):936-48. doi: 10.1016/j.neuroimage.2007.09.024. Epub 2007  
938 Sep 21. PMID: 17997329.
- 939 44. Lorthois S, Cassot F, Lauwers F. Simulation study of brain blood flow regulation by intra-  
940 cortical arterioles in an anatomically accurate large human vascular network: Part I:  
941 methodology and baseline flow. *Neuroimage*. 2011 Jan 15;54(2):1031-42. doi:  
942 10.1016/j.neuroimage.2010.09.032. Epub 2010 Oct 15. PMID: 20869450.
- 943 45. Markuerkiaga I, Barth M, Norris DG. A cortical vascular model for examining the specificity of  
944 the laminar BOLD signal. *Neuroimage*. 2016 May 15;132:491-498. doi:  
945 10.1016/j.neuroimage.2016.02.073. Epub 2016 Mar 4. PMID: 26952195.
- 946 46. Markuerkiaga I, Marques JP, Bains LJ, Norris DG. An in-vivo study of BOLD laminar responses  
947 as a function of echo time and static magnetic field strength. *Sci Rep*. 2021 Jan 21;11(1):1862.  
948 doi: 10.1038/s41598-021-81249-w. PMID: 33479362; PMCID: PMC7820587.
- 949 47. Norris DG, Polimeni JR. Laminar (f)MRI: A short history and future prospects. *Neuroimage*.  
950 2019 Aug 15; 197:643-649. doi: 10.1016/j.neuroimage.2019.04.082. Epub 2019 May 3. PMID:  
951 31059800.
- 952 48. Norris DG. Spin-echo fMRI: The poor relation? *Neuroimage*. 2012 Aug 15;62(2):1109-15. doi:  
953 10.1016/j.neuroimage.2012.01.003. Epub 2012 Jan 8. PMID: 22245351.
- 954 49. Ogawa S, Menon RS, Tank DW, Kim SG, Merkle H, Ellermann JM, Ugurbil K. Functional brain  
955 mapping by blood oxygenation level-dependent contrast magnetic resonance imaging. A  
956 comparison of signal characteristics with a biophysical model. *Biophys J*. 1993 Mar;64(3):803-  
957 12. doi: 10.1016/S0006-3495(93)81441-3. PMID: 8386018; PMCID: PMC1262394.
- 958 50. Olman CA, Harel N, Feinberg DA, He S, Zhang P, Ugurbil K, Yacoub E. Layer-specific fMRI  
959 reflects different neuronal computations at different depths in human V1. *PLoS One*.

- 960 2012;7(3):e32536. doi: 10.1371/journal.pone.0032536. Epub 2012 Mar 20. PMID: 22448223;  
961 PMID: PMC3308958.
- 962 51. Palomero-Gallagher N, Zilles K. Cortical layers: Cyto-, myelo-, receptor- and synaptic  
963 architecture in human cortical areas. *Neuroimage*. 2019 Aug 15;197:716-741. doi:  
964 10.1016/j.neuroimage.2017.08.035. Epub 2017 Aug 12. PMID: 28811255.
- 965 52. Park H. Polytope bounded Voronoi diagram in 2D and 3D. Github. 2021.  
966 <https://github.com/hyongju/Polytope-boundedVoronoi-diagram/releases/tag/1.15>
- 967 53. Petridou N, Siero JCW. Laminar fMRI: What can the time domain tell us? *Neuroimage*. 2019  
968 Aug 15; 197:761-771. doi: 10.1016/j.neuroimage.2017.07.040. Epub 2017 Jul 20. PMID:  
969 28736308; PMID: PMC5775945.
- 970 54. Pfaffenrot V, Koopmans PJ. Magnetization transfer weighted laminar fMRI with multi-echo  
971 FLASH. *Neuroimage*. 2022 Dec 1; 264:119725. doi: 10.1016/j.neuroimage.2022.119725.  
972 Epub 2022 Oct 31. PMID: 36328273.
- 973 55. Pfaffenrot V, Voelker MN, Kashyap S, Koopmans PJ. Laminar fMRI using T2-prepared multi-  
974 echo FLASH. *Neuroimage*. 2021 Aug 1; 236:118163. doi:  
975 10.1016/j.neuroimage.2021.118163. Epub 2021 May 21. PMID: 34023449.
- 976 56. Pflugfelder D, Vahedipour K, Uludağ K, Shah NJ, Stöcker T. On the numerically predicted  
977 spatial BOLD fMRI specificity for spin echo sequences. *Magn Reson Imaging*. 2011  
978 Nov;29(9):1195-204. doi: 10.1016/j.mri.2011.07.015. Epub 2011 Sep 13. PMID: 21917392.
- 979 57. Polimeni JR, Fischl B, Greve DN, Wald LL. Laminar analysis of 7T BOLD using an imposed  
980 spatial activation pattern in human V1. *Neuroimage*. 2010 Oct 1;52(4):1334-46. doi:  
981 10.1016/j.neuroimage.2010.05.005. Epub 2010 May 9. PMID: 20460157; PMID:  
982 PMC3130346.
- 983 58. Polimeni JR, Uludağ K. Neuroimaging with ultra-high field MRI: Present and future.  
984 *Neuroimage*. 2018 Mar; 168:1-6. doi: 10.1016/j.neuroimage.2018.01.072. Epub 2018 Feb 1.  
985 PMID: 29410013.
- 986 59. Poplawsky AJ, Fukuda M, Kim SG. Foundations of layer-specific fMRI and investigations of  
987 neurophysiological activity in the laminarized neocortex and olfactory bulb of animal models.  
988 *Neuroimage*. 2019 Oct 1;199:718-729. doi: 10.1016/j.neuroimage.2017.05.023. Epub 2017  
989 May 12. PMID: 28502845; PMID: PMC5682230.
- 990 60. Pries AR, Neuhaus D, Gaehtgens P. Blood viscosity in tube flow: dependence on diameter  
991 and hematocrit. *Am J Physiol*. 1992 Dec;263(6 Pt 2):H1770-8. doi:  
992 10.1152/ajpheart.1992.263.6.H1770. PMID: 1481902.
- 993 61. Puckett AM, Aquino KM, Robinson PA, Breakspear M, Schira MM. The spatiotemporal  
994 hemodynamic response function for depth-dependent functional imaging of human cortex.

- 995 Neuroimage. 2016 Oct 1; 139:240-248. doi: 10.1016/j.neuroimage.2016.06.019. Epub 2016  
996 Jun 15. PMID: 27321045.
- 997 62. Reichold J, Stampanoni M, Keller AL, Buck A, Jenny P, Weber B. Vascular graph model to  
998 simulate the cerebral blood flow in realistic vascular networks. *Journal of Cerebral Blood Flow*  
999 *& Metabolism*. 2009 Aug;29(8):1429-43.
- 1000 63. Risser L, Plouraboué F, Steyer A, Cloetens P, Le Duc G, Fonta C. From homogeneous to  
1001 fractal normal and tumorous microvascular networks in the brain. *J Cereb Blood Flow Metab*.  
1002 2007 Feb;27(2):293-303. doi: 10.1038/sj.jcbfm.9600332. Epub 2006 May 24. PMID:  
1003 16736048.
- 1004 64. Roefs E, Schellekens W, Báez-Yáñez MG, Bhogal A, Groen I, van Osch M, Siero J, Petridou  
1005 P. The Contribution of the Vascular Architecture and Cerebrovascular Reactivity to the BOLD  
1006 signal Formation across Cortical Depth (2024) *Imaging Neuroscience, in press*
- 1007 65. Safaeian N, Sellier M, David T. A computational model of hemodynamic parameters in cortical  
1008 capillary networks. *J Theor Biol*. 2011 Feb 21;271(1):145-56. doi: 10.1016/j.jtbi.2010.11.038.  
1009 Epub 2010 Dec 2. PMID: 21130099.
- 1010 66. Schellekens W, Bhogal AA, Roefs EC, Báez-Yáñez MG, Siero JC, Petridou N. The many  
1011 layers of BOLD. The effect of hypercapnic and hyperoxic stimuli on macro- and micro-vascular  
1012 compartments quantified by CVR, M, and CBV across cortical depth. *J Cereb Blood Flow*  
1013 *Metab*. 2023 Mar;43(3):419-432. doi: 10.1177/0271678X221133972. Epub 2022 Oct 19.  
1014 PMID: 36262088; PMCID: PMC9941862.
- 1015 67. Schmid F, Barrett MJP, Jenny P, Weber B. Vascular density and distribution in neocortex.  
1016 *Neuroimage*. 2019 Aug 15; 197:792-805. doi: 10.1016/j.neuroimage.2017.06.046. Epub 2017  
1017 Jun 29. PMID: 28669910.
- 1018 68. Siero JC, Petridou N, Hoogduin H, Luijten PR, Ramsey NF. Cortical depth-dependent temporal  
1019 dynamics of the BOLD response in the human brain. *J Cereb Blood Flow Metab*. 2011  
1020 Oct;31(10):1999-2008. doi: 10.1038/jcbfm.2011.57. Epub 2011 Apr 20. PMID: 21505479;  
1021 PMCID: PMC3208150.
- 1022 69. Siero JC, Ramsey NF, Hoogduin H, Klomp DW, Luijten PR, Petridou N. BOLD specificity and  
1023 dynamics evaluated in humans at 7 T: comparing gradient-echo and spin-echo hemodynamic  
1024 responses. *PLoS One*. 2013;8(1):e54560. doi: 10.1371/journal.pone.0054560. Epub 2013 Jan  
1025 15. PMID: 23336008; PMCID: PMC3546000.
- 1026 70. Tsai PS, Kaufhold JP, Blinder P, Friedman B, Drew PJ, Karten HJ, Lyden PD, Kleinfeld D.  
1027 Correlations of neuronal and microvascular densities in murine cortex revealed by direct  
1028 counting and colocalization of nuclei and vessels. *J Neurosci*. 2009 Nov 18;29(46):14553-70.  
1029 doi: 10.1523/JNEUROSCI.3287-09.2009. PMID: 19923289; PMCID: PMC4972024.

- 1030 71. Uludağ K, Blinder P. Linking brain vascular physiology to hemodynamic response in ultra-high  
1031 field MRI. *Neuroimage*. 2018 Mar; 168:279-295. doi: 10.1016/j.neuroimage.2017.02.063.  
1032 Epub 2017 Feb 22. PMID: 28254456.
- 1033 72. Uludağ K, Müller-Bierl B, Uğurbil K. An integrative model for neuronal activity-induced signal  
1034 changes for gradient and spin echo functional imaging. *Neuroimage*. 2009 Oct 15;48(1):150-  
1035 65. doi: 10.1016/j.neuroimage.2009.05.051. Epub 2009 May 27. PMID: 19481163.
- 1036 73. Uludağ K. Physiological modeling of the BOLD signal and implications for effective  
1037 connectivity: A primer. *Neuroimage*. 2023 Aug 15;277:120249. doi:  
1038 10.1016/j.neuroimage.2023.120249. Epub 2023 Jun 24. PMID: 37356779.
- 1039 74. Van Horen TWP, Siero JCW, Bhogal AA, Petridou N, Báez-Yáñez MG. Microvascular  
1040 Specificity of Spin Echo BOLD fMRI: Impact of EPI Echo Train Length. *bioRxiv [Preprint]*. 2023  
1041 Sep 15:2023.09.15.557938. doi: 10.1101/2023.09.15.557938. PMID: 37745507; PMCID:  
1042 PMC10516014.
- 1043 75. Viessmann O, Scheffler K, Bianciardi M, Wald LL, Polimeni JR. Dependence of resting-state  
1044 fMRI fluctuation amplitudes on cerebral cortical orientation relative to the direction of B0 and  
1045 anatomical axes. *Neuroimage*. 2019 Aug 1;196:337-350. doi:  
1046 10.1016/j.neuroimage.2019.04.036. Epub 2019 Apr 17. PMID: 31002965; PMCID:  
1047 PMC6559854.
- 1048 76. Vizioli L, Moeller S, Dowdle L, Akçakaya M, De Martino F, Yacoub E, Uğurbil K. Lowering the  
1049 thermal noise barrier in functional brain mapping with magnetic resonance imaging. *Nat*  
1050 *Commun*. 2021 Aug 30;12(1):5181. doi: 10.1038/s41467-021-25431-8. PMID: 34462435;  
1051 PMCID: PMC8405721.
- 1052 77. Vovenko E. Distribution of oxygen tension on the surface of arterioles, capillaries and venules  
1053 of brain cortex and in tissue in normoxia: an experimental study on rats. *Pflugers Arch*. 1999  
1054 Mar;437(4):617-23. doi: 10.1007/s004240050825. PMID: 10089576.
- 1055 78. Weber B, Keller AL, Reichold J, Logothetis NK. The microvascular system of the striate and  
1056 extrastriate visual cortex of the macaque. *Cereb Cortex*. 2008 Oct;18(10):2318-30. doi:  
1057 10.1093/cercor/bhm259. Epub 2008 Jan 24. PMID: 18222935.
- 1058 79. Weisskoff RM, Zuo CS, Boxerman JL, Rosen BR. Microscopic susceptibility variation and  
1059 transverse relaxation: theory and experiment. *Magn Reson Med*. 1994 Jun;31(6):601-10. doi:  
1060 10.1002/mrm.1910310605. PMID: 8057812.
- 1061 80. Yablonskiy DA, Sukstanskii AL. Theoretical models of the diffusion weighted MR signal. *NMR*  
1062 *Biomed*. 2010 Aug;23(7):661-81. doi: 10.1002/nbm.1520. PMID: 20886562; PMCID:  
1063 PMC6429954.

1064 81. Zhao F, Wang P, Hendrich K, Ugurbil K, Kim SG. Cortical layer-dependent BOLD and CBV  
1065 responses measured by spin-echo and gradient-echo fMRI: insights into hemodynamic  
1066 regulation. *Neuroimage*. 2006 May 1;30(4):1149-60. doi: 10.1016/j.neuroimage.2005.11.013.  
1067 Epub 2006 Jan 18. PMID: 16414284.